Nanoscale characterization of graphene and polymer blends using tip-enhanced Raman spectroscopy and 3D surface-enhanced Raman spectroscopy

A Thesis for the Degree
of
Doctor of Science

Submitted to
School of Science & Technology
Kwansei-Gakuin University

By

Sanpon Vantasin

in February 2016

Contents

Introduction 1

General introduction 1

Raman Spectroscopy 1

Diffraction Limit 4

Super-resolution Raman spectroscopy 5

Surface-enhanced Raman scattering spectroscopy (SERS) 8

Tip-enhanced Raman scattering spectroscopy (TERS) 10

Grapene and graphene nanostructure 12

References 14

Chapter 1: Tip-Enhanced Raman Scattering of the Local Nanostructure of Epitaxial Graphene Grown on 4H-SiC $(000\bar{1})$ 19

Abstract 20

Introduction 20

Experimental Section 22

Results and Discussion 23

Conclusions 29

References 30

Chapter 2: Characterization of SiC-grown epitaxial graphene microisland using tip-enhanced Raman spectroscopy 37

Abstract 38

Introduction 38

Experimental Section 40

Results and Discussion 42

Conclusions 46

References 46

Chapter 3: 3D SERS imaging using chemically-synthesized highly-symmetric nanoporous silver microstructure 54

Abstract 55

Introduction, result, and discussion 55

Experimental Section 60

References 62

Acknowledgements 68

List of Publications 69

Abbreviations and symbols

AFM	atomic Force Microscopy
ATR	attenuated total reflection
FWHM	full-width half maxima
IR	infrared (spectroscopy)
iTO	in-plane transverse optical
LO	longtitudinal
LSPR	localized surface plasmon resonance
µm	micrometer
NIR	near-infrared (spectroscopy)
nm	nanometer
PHB	polyhydroxybutyrate
PDLLA	poly(D,L)lactic acid
PS	polystyrene
PVP	polyvinylpyrrolidone
SERS	surface enhanced Raman scattering
SiC	silicon carbide
SNOM	scanning near field optical microscopy
TERS	tip-enhanced Raman scattering
UV	ultraviolet

E	electric field/energy
ε	dielectric constant
γ	Grüneisen parameter
H	Planck constant
I	intensity
λ	wavelength
n	refractive index
NA	numerical aperture
ω	angular frequency

General introduction

This thesis explores the use of near field probe, e.g. silver nanotips and hierarchical silver microparticles to investigate nanoscale features of graphene and polymer blends. The main underlying reason of the near-field probes is the limited spatial resolution of conventional Raman spectroscopy, which is diffraction limit of light,[1] and in the case of Raman spectroscopy in polymer, the laser spot expansion from refraction.[2] Diffraction limit is dependent on various factors which will be discussed in the following sections, but is practically around 300 nm.[3] This limit is a great hindrance to the characterization of nanomaterials, since many important nanoscale features has the size of less than 100 nm. The resolution limit larger than the features means each features cannot be probed individually, and preventing the study of some 'hidden' properties of the nanomaterials. Many researchers developed creative and promising methods to break through this limit, which will be discussed in this chapter. Tip-enhanced Raman spectroscopy, a class of techniques among the diffraction limit-breaking methods, is a focus of this thesis, and it was used to attain nanoscale characterization of nanofeatures on novel materials such as graphene. Another focus of this thesis is about 3D SERS imaging on symmetric 3D SERS substrate, which not only improves spatial resolution in polymer, but also provides the 3D vibrational information in polymer systems.

Raman spectroscopy

Raman spectroscopy relies on the effect of Raman scattering, which is a scattering interaction between electromagnetic wave and chemical bond vibration. Since each molecule has unique bond formations, the interaction is unique for each chemical. This characteristic provides distinctive Raman spectrum and allows characterizations of samples.[4]

The principle of Raman scattering process is well-covered elsewhere.[4–6] Briefly, chemical bond vibrations can be represented as anharmonic dipole oscillator. Due to the wave-particle duality, the allowed energy levels of the vibration are quantized. The allowed level can be presented by the equation:

$$E_{vib} = hf(v + \frac{1}{2}) + h\chi f(v + \frac{1}{2})^2$$

where v is vibrational quantum number, f is base vibration frequency, h is Planck constant, and χf denotes magnitude of anharmonicity.[5]

Raman scattering is a scattering process of photon with bonds. In most case, the scattering is elastic and results in Rayleigh scattering. However, if there is energy transfer in the process (i.e. inelastic scattering), the bond vibrational level would change, and the scattered photon would loss or gains the corresponding energy.[7] The selection rule of this process is $\Delta v = 1$ and $\Delta J = 0, \pm 2$, where J is rotational quantum number. The energy level diagram for a comparison of Raman scattering to other spectroscopic process is shown in Figure 1.

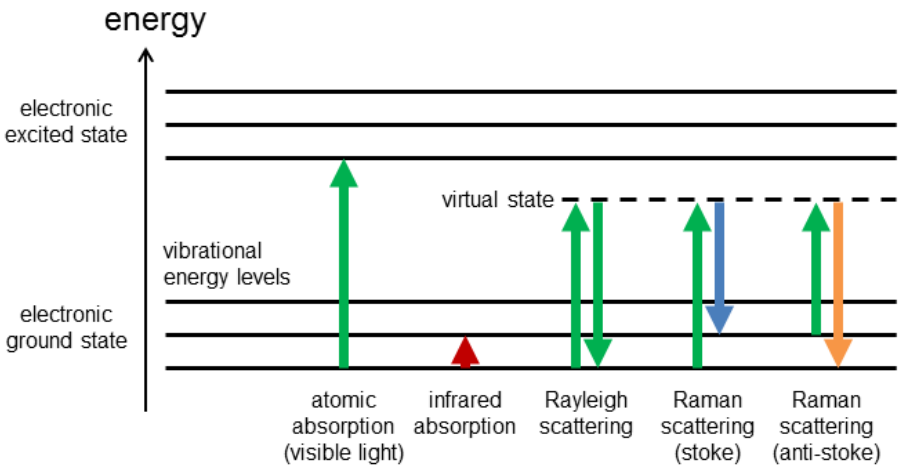

Figure 1 Energy level diagram of simple spectroscopic process. Drawn using MS Powerpoint with Figure 1 of Reference 8 as an example.

In classical physics viewpoint, electric field of photon induces dipole moment in molecule. The magnitude of induced dipole is proportional to electrical polarizability of molecule. By considering the vibration as a combination of orthogonally normal vibration modes, the scattering effect on each vibration can be considered separately. The scattering process is often represented by this equation:[7–9]

$$\mu = \alpha_0 E_0 cos2\pi f_0 t + \frac{1}{2}\left(\frac{\partial\alpha}{\partial Q_i}\right)_0 Q_{i0} E_0 cos2\pi t(f_0 - f_i) + \frac{1}{2}\left(\frac{\partial\alpha}{\partial Q_i}\right)_0 Q_{i0} E_0 cos2\pi t(f_0 + f_i)$$

where μ is the induced dipole moment, α is polarizability, α_0 is the initial polarizability without vibration, E_0 is the electric field amplitude of photon, f_0 is frequency of photon, f_i is frequency change after the scattering, Q_i is the position in normal coordinate of the vibration, and Q_{i0} is the initial (middle) position in the coordinate of the vibration.

One can see that the photon frequency changes (i.e. energy transfer) only in the second and third term. If the vibration does not change polarizability of molecule, the term $\left(\frac{\partial\alpha}{\partial Q_i}\right)_0$ would be zero, and the second and third term would be disappeared, and there would be no energy transfer. Thus, the first term represent Rayleigh scattering (elastic). The second term where photon loss energy represent Stoke Raman scattering, while the third term represent anti-stoke Raman scattering. This criterion of polarizability change is useful to explain the reason that some vibrational modes appear in infrared absorption spectra, but not in Raman spectra.[7–9]

In practice, Raman spectroscopy is much less problematic when encountering sample with water content, comparing to infrared absorption spectroscopy. The optic setup for Raman spectroscopy also relatively easy since the electromagnetic wave in the process is in in visible Region. Raman spectroscopy have been used in many fields of research and industry, including but not limited to organic chemistry[10–13], materials science[14,15], biological sciences[16–18], polymers[19–21], and also graphene and related materials[22–28].

Diffraction Limit

Many modern Raman spectrometers (and also similar spectrometer such as IR, NIR) are equipped with microscope to acquire the signal from a small spot. Obviously, any simple aberrations of optical microscope (e.g. spherical aberration, coma, distortion, etc.) would also apply to the Raman spectrometer as well, and thus the quality of optic setup would limit the spatial resolution.[29] Nevertheless, even with the ideal setup with minimal aberration, there is another barrier, which is the diffraction of light. Ernst Abbe in 1873 and Hermann von Helmhotz in a year later made a mathematical approach of this limit using objective lens and grating (Figure 1).

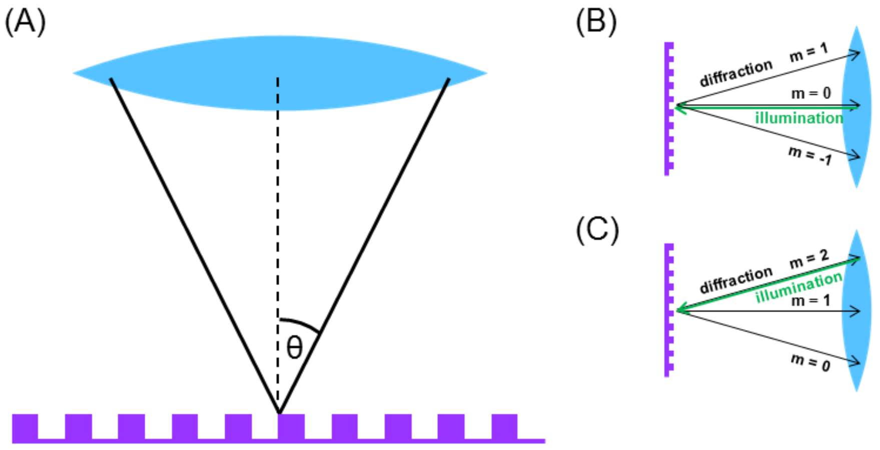

Figure 2 Schema of the setup in Abby's consideration of diffraction limit. Objective lens and grating (A), together with the consideration in the case of (B) perpendicular illumination and (C) angled illumination. Drawn using MS Powerpoint with Figure 4 of Reference 29 as an example.

Abbe argue that each unit of grating could be resolved by the microscope if one could detect the first diffraction maxima (aside from central maxima).[30] When considering illumination perpendicular to grating plane (Figure 1B), the minimum grating spacing (d) which the first maxima can be detected is denoted by:

$$d = \frac{\lambda}{n\sin(\theta)} = \frac{\lambda}{NA}$$

where λ is the wavelength of the illumination, n is the refractive index of the objective lens, θ is the half angle of light cone, and NA is the numerical aperture of the objective lens.[30] However, when considering angled illumination (Figure 1C), the smaller d can be acquired. When the same lens is used in both illumination and signal collection, the equation becomes the Abby's formula of diffraction limit:

$$d = \frac{\lambda}{2NA}$$

With 555 nm illumination and objective lens with 0.9 NA, the diffraction limit is about 308 nm, thus the practical diffraction limit around 300 nm previously stated.

Since the diffraction is a fundamental property of light waves, this limit cannot be overcome with conventional setup of optical parts. No matter how much the magnification is, the detail of samples smaller than this limit cannot be resolved, and the output image just appears larger without additional details. The magnification beyond this useful point is often called 'empty magnification'.[31]

In microscopy, this limit was easily surpassed by replacing light wave with electron. Electron wavelength in picometers scale can be attained by standard electron microscope.[32] However, in Raman spectroscopy, the wavelength around visible region is needed, and thus other methods are required to break through this limit and achieve nanoscale characterization of material with Raman spectroscopy.

Super-resolution Raman spectroscopy

From the equation of diffraction limit, the two simple pathways to decrease the limit are to increase NA of objective lens and decrease wavelength. High-NA objectives lens are commercially available in the form of oil-immersion lens, with NA as high as 1.4 being very feasible. The use of high NA lens is a basic which can be combined with following resolution-improving technique.[33–35] The other basic pathway, decreasing wavelength, have been realized in UV-Raman. With the smaller wavelength of ultraviolet light, a spatial resolution of 150 nm was demonstrated.[35] Attenuated total reflection (ATR) mode Raman spectroscopy also reduces wavelength of visible excitation laser by using high refractive index medium such as ZnSe (n = 2.6), and thus improving spatial resolution.[36] It should be mentioned that although UV and ATR Raman spectroscopy can improve spatial resolution, it is not the main purpose of the techniques. Ultraviolet excitation allows resonance Raman effect for samples with high energy gap between electronic ground state and excitation state (e.g. polycyclic aromatic hydrocarbon and amino acids).[37] ATR mode penetrates only small depth from surface of the sample, allowing surface and interface study.[36]

To further improve the spatial resolution, near-field techniques were utilized.[38] By placing the illumination or collection very close to the probing spot, diffraction can be restrained. A notable method without using complex mechanism is to use dielectric microsphere as a near-field lens, which demonstrates the Raman measurement with spatial resolution of 80 nm.[39] Scanning near-field optical microscopy (SNOM), also called as Near field scanning optical microscopy (NSOM) is one of the few techniques which provide spatial resolution for Raman spectroscopy down to single molecular level.[40,41] The principle of SNOM is to utilize the nanoscale manipulation capability of scanning probe microscopy (SPM) such as scanning tunneling microscopy (STM) or atomic force microscope (AFM) by control tips with nanometers size apex to the target, then use the geometry of the tips to confine probing area of optical microscope.[40–44] Figure 2 presents a basic view of SNOM, the diffracted light is blocked (in the case of aperture SNOM) or prevented from the light path (ATR SNOM or scattering SNOM).

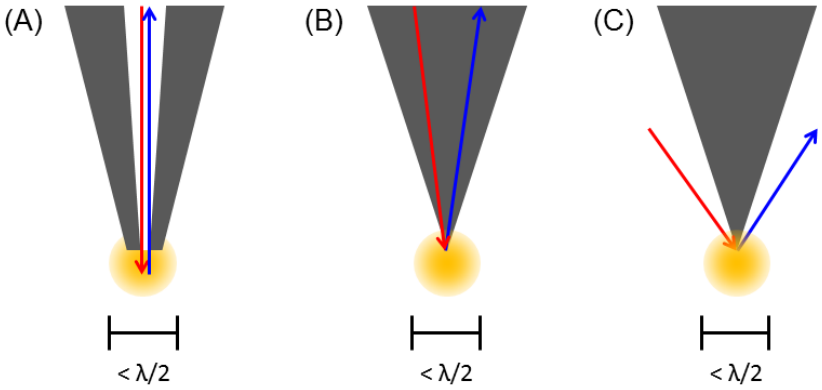

Figure 3 Examples of typical setups of SNOM. (A) Aperture SNOM, (B) ATR SNOM, and (C) scattering SNOM. Noted that the SNOM approach can be used in just illumination, just collection, or both. Drawn with MS Powerpoint using explanation from Reference 39-43.

By mostly eliminate the effects from diffraction, the spatial resolution is improved dramatically. SNOM based Raman spectroscopy have been used to perform nanoscale characterizations of human cells[45], fossils[46], damaged silicon wafer[47], CVD-diamond layers[48], and carbon nanomaterials[49], all with spatial resolutions of 100 nm or better. SNOM can be used with other microscopy and spectroscopy as well as Raman.[40,41]

Localized surface plasmon resonance (LSPR) is an interaction between electron cloud in material and electric field of incoming light wave.[50] For electromagnetic wave in visible region, LSPR is easily achievable by nanoparticles/nanostructure of noble metal such as silver and gold.[50] LSPR produces two important effects to this topic, immense enhancement in nanoscale distance from the metal surface[50,51] and wavelength contraction[52], both effects, with proper environment, can greatly improve spatial resolution in Raman measurement.[1,3,53] The plasmon resonance enhancement-assisted Raman spectroscopy is the basic of surface enhance Raman scattering spectroscopy (SERS), while scattering SNOM with SERS is the principle of tip-enhanced Raman scattering spectroscopy (TERS). These two techniques are the main focus of this thesis. With TERS, spatial resolution down to few nanometers or even sub-nanometers is feasible.[54–58]

It is worthy to note that SNOM with LSPR can also be used with techniques other than

Raman spectroscopy. For example, visible/IR optical microscopy with spatial resolution of 10 nm was demonstrated.[59,60]

Surface-enhanced Raman scattering spectroscopy (SERS)

Surface-enhanced Raman scattering spectroscopy is a technique which relies on an enhancement effect when target molecule is in a vicinity of certain materials. There are two mechanism which is involved in Raman signal enhancement, electromagnetic enhancement mechanism and chemical enhancement mechanism.[61] The materials which can enhance the Raman signal are called SERS substrate. Since the enhancement can be as high as million to billion times, SERS allows ultrasensitive detection of chemical and biological substance. Trace contaminant with concentration as low as 10^{-15} M can be detected using SERS.[62] Trinitrotoluene (TNT)[63], DNA[64], mercury[65], and proteins[66] with concentration in nanomolar to attomolar range can be detected using SERS.

Fleischmann, Hendra and McQuillan observed SERS effect on 1974, but they explained as it was high surface area that provided unusually high Raman signal of pyridine on unsmooth silver substrate.[67,68] Jeanmaire and Van Duyne[69], and also Albrecht and Creighton[70] later clarified that the high signal was a result of electric field enhancement by silver structure. The origin of electric field enhancement is LSPR between light and electron cloud in metal nanostructure as explained in the previous section. SERS was solely explained by electromagnetic enhancement mechanism until the discovery of chemical enhancement mechanism.[71–73] Some molecules have been found to have 10-1000 times enhancement factor compare to the others, and this phenomenon is substrate dependent, such as pyridine and piperidine on silver.[74] The process of chemical enhancement mechanism is explain as when molecules adsorbed on a substrate, charge-transfer between energy level of molecules and the substrate is possible via Herzberg-Teller vibronic coupling. This allows a resonance Raman-like effect, which enhance scattering signal.[61,74] This mechanism allows SERS effect on other interesting material beside noble metal, for example, semiconductor.[48,75]

The magnitude of LSPR electric enhancement around spherical metallic nanoparticle can be represent by the equation[50,76]:

$$E_{out}(x,y,z) = E_0\hat{z} - \left[\frac{\varepsilon_{in} - \varepsilon_{out}}{(\varepsilon_{in} - 2\varepsilon_{out})}\right] a^3 E_0 \left[\frac{\hat{z}}{r^3} - \frac{3z}{r^5}(x\hat{x} + y\hat{y} + z\hat{z})\right]$$

where E_{out} is the enhanced electric field vector, E_0 is the magnitude of electric field of incoming photon, ε_{in} is complex dielectric constant of metal, ε_{out} is complex dielectric constant of the surrounding medium, a is particle size, x, y, and z is position in the corresponding axis, and $\hat{x}$, $\hat{y}$, and $\hat{z}$ is unit vector in the corresponding axis.

This equation provides many useful physical meanings. First, if the real part of ε_{in} is close to $-2\varepsilon_{out}$ and its imaginary part is near-zero, the $(\varepsilon_{in} - 2\varepsilon_{out})$ in the denominator would approaches zero, resulting in extremely high value of the overall term. This is possible in the case when the particle is silver or gold, as the two metals provide negative real part of dielectric constant in visible wavelength region. Since dielectric constant is highly dependent on wavelength, only small region of wavelength would give near-zero $(\varepsilon_{in} - 2\varepsilon_{out})$ value and extreme field enhancement. This is the background of the word "resonance" in the process name. For small metal particle in water, the resonance wavelength is around 400 nm for silver and 520 nm for gold. Second, enhancement from LSPR is strongly geometry dependent. The size of particle a has power of 3 in the equation. The shape of particle also crucial because the form of the equation would change drastically in the case of non-spherical particles. Third, the term r^3 and r^5 in the denominator indicate the field enhancement is very strong near the particle surface and is quickly weaken as the distance from the particle increases.

Since LSPR is highly localized and SERS signal is immensely high compared to normal Raman scattering, the signal from sample within small area of enhanced electric field can overwhelm the signal from neighbor area. This spot is called "hot spot".[76,77] This effect can provide a very high spatial resolution if the exact position of hot spot is known. However, even though SERS can provide Raman signal from spot smaller than diffraction limit, if there are many hot spot together in large groups, diffraction limit cannot be exceeded because the signal is an average from spots over a large area. Moreover, even in the case of SERS with single nanoparticle (i.e. single hot spot), if the precise position of the particle is not certain, one need to do SERS mapping to find the position. In this case, hot spot would appear as large as diffraction limit because Abby's criterion also applies for self-luminous sample.[30] In order to realize and control the position of hotspot, SERS probe can be attached to SPM, and this is the origin of TERS.

There are studies of using SERS to get improved spatial resolution. Tracking of free-floating gold nanoparticles in cells and repeating SERS measurement provides Raman spectra of intracellular pathway.[78] In Chapter 3 of this thesis, SERS effect is used to improved spatial resolution in Z axis, which is a problem for Raman spectroscopy within polymers. These two studies achieve good spatial resolution, but not surpassing diffraction limit.

Tip-enhanced Raman scattering spectroscopy (TERS)

TERS is a combination of SERS and SNOM, but SERS substrate in a form of nanotips connected to SPM instrument is used instead of nanoparticles/nanostructure under samples. As in SERS, the Raman signal enhancement arises from near-field enhancement of electric field via LSPR interaction between metallic nanostructures and incident light. In the case of TERS, the nanostructures are nano-sized apex of metallic tip. From the equation of LSPR near-field enhancement, one can see that the enhancement is very strong in the small distance near the enhancing surface, but decrease drastically as the distance increase. Thus, enhancement by nanotips is confined to the small volume at the tip apex. 'Lighting rod effect' also contributes to the electric field enhancement and confinement at the tip apex.[79] Due to the confinement, this enhancement can provide SERS signal with nanoscale spatial resolution, exceeding diffraction limit of light. Resolution of 1.7 nm can archived in ambient condition (room temperature, normal pressure).[54] With ultrahigh vacuum and low temperature, even subnanometer resolution is possible.

Since the enhancement mechanism of TERS is the same as SERS, all principle of SERS also applies. The material of the tip must be compatible with the wavelength of incident laser. For example, silver tips are normally used in TERS experiment with 514 nm or 532 nm excitation lasers while gold tips are compatible with laser wavelength in the region of 600-700 nm (often 632.8 nm helium-neon laser). Topology of tips also drastically affects the enhancement factor.[80,81]

An advantage of TERS is that it provides both topological information from SPM and molecular vibration from Raman spectroscopy. The correlation between the two information is highly valuable for nanomaterial characterization. With the exceeding spatial resolution, TERS have been used to study nanoscale photocatalytic reaction[82], sub-molecular photochemistry[57], adsorbed species on single-crystal surface[83], and nanomaterial such as GaN nanowires[1], nanotransistors[84], polymer nanocomposite[27,85], carbon nanotube[3,54,86–88], and graphene[34,89–100].

In practice, TERS experiments come with various setup and instrumentation. The illumination mode can be from top, side, or bottom. The tip control scheme can be AFM, which is compatible with almost all sample, or STM, which can adjust tip-sample distance. The material of the tip can be gold for chemical stability or silver for slightly higher enhancement. Tip can also be etched bulk metal tip or metal-coated AFM tip. A notable setup is gap mode TERS, which is performed by placing the sample on SERS-active substrate (usually gold or silver flim) and position TERS tip on the top. The gap created by the tip and substrate provides additional enhancement about 100 times to TERS signal.[1,53,86] Figure 4 represent electric field enhancement in gap-mode TERS from finite-difference time-domain calculation with 40 nm tip apex, 3 nm silver tip-silver plate distance, and 514 nm excitation wavelength.

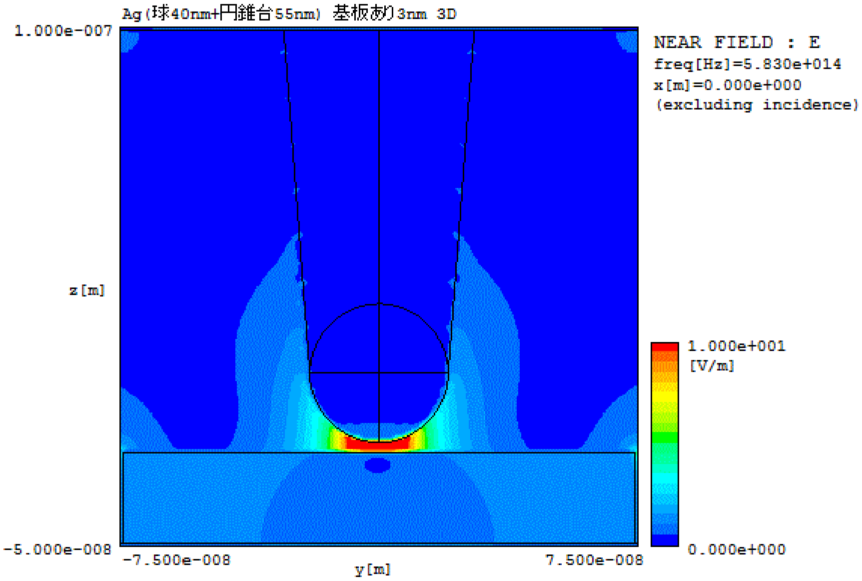

Figure 4 FDTD calculation showing electric field enhancement in gap-mod TERS

Recent advances in TERS development includes low-temperature low-pressure TERS[57,101], which significantly reduce the problem from thermal drift, high-enhancement advance tips such as rough surface tips[80] and bowtie nanoantenna tip with self-producing gap mode[81], synchronize tip tapping- Raman measurement which allows near-field and far-field measurement in a single run[33], Wave-guided tip[102], pressure-assisted TERS[56], and electrochemical TERS[103,104].

The studies in this thesis do not involved in the development of TERS, but an application of TERS in a characterization of nanomaterial was demonstrated. In Chapter 1, TERS was used to reveal the properties and formation mechanism of nanostructures on epitaxial graphene. In Chapter 2, similar structures were studied, but on graphene micoisland, which allows a further discussion of established and alternate mechanism for nanostructures formation.

Grapene and graphene nanostructure

Graphene is a novel nanometerials with a large number of unique and interesting properties. Graphene have been shown to have zero band gap[105,106], tunable band gap[107,108], quantum hall effects[109,110], ballistic transport[111], extremely high tensile strength and Young's modulus[112], Raman enhancement capability[113–115], large surface area[116], transparency[117], etc. Due to these impressive properties, graphene have been demonstrate to be a promising material in high-speed electronics[116], ultrafast photodetector[118], very high-frequency transistor[119], and supercapacitor[120–122].

In order to build high-quality graphene device, a production of large amount of high-quality graphene sheet is a crucial key factor. The most well-known method for graphene synthesis, the "scotch tape" exfoliation of highly ordered pyrolysis graphene provide graphene sheet with minimal defect, but it can only produce small flake of graphene.[111,123] Scotch tape peeling also require a lot of manual labor which is difficult to practice in large-scale. The liquid oxidation exfoliation method convert graphite into graphite oxide, cleaving between the flakes of graphene oxide and then reduces them back into graphene.[124–126] This method can produces large number of graphene sheet but contains large amount of defects. Chemical vapor deposition of methane on metal and on-SiC epitaxial growth can produce low-defect, wafer-size graphene sheet. Both method can also easily scale up to mass scale. However, epitaxial-grown graphene has an advantage over CVD graphene, as SiC is an electrical insulator. Thus, graphene grown on SiC does not need a substrate transfer process to be used in electric circuit.

TERS have been used to characterize graphene in nanoscale level. Number of layers[34,92–94,96,98], defects[91,95], stress change[28], Raman modes suppression[97], edges[99,100], and deposited foreign chemical of graphene[89,90,127] have all been investigated with great spatial resolution. However, before the studies in this thesis, there is no TERS study on important nanostructures of graphene such as nanoridges and nanosteps.

The instrument used in TERS studies in this thesis is special and very suitable for nanostructures study, as it control TERS tip by non-contact mode AFM. STM-TERS is not suitable for this study because undoped SiC is not conductive. TERS measurement of the structures by contact or tapping mode AFM TERS is also disputable because tip-graphene interaction might interfere the true nature of graphene.

References

(1) Domke, K. F.; Pettinger, B. Studying Surface Chemistry beyond the Diffraction Limit: 10 Years of TERS. *ChemPhysChem* **2010**, *11* (7), 1365–1373.

(2) Everall, N. J. Confocal Raman Microscopy: Why the Depth Resolution and Spatial Accuracy Can Be Much Worse than You Think. *Appl. Spectrosc.* **2000**, *54* (10), 1515–1520.

(3) Verma, P.; Ichimura, T.; Yano, T.; Saito, Y.; Kawata, S. Nano-Imaging through Tip-Enhanced Raman Spectroscopy: Stepping beyond the Classical Limits. *Laser Photonics Rev.* **2009**, *4* (4), 548–561.

(4) Miller, F. A.; Mayo, D. W.; Hannah, R. W. *Course Notes on the Interpretation of Infrared and Raman Spectra*; Wiley-Interscience: Hoboken, N.J, 2004.

(5) Larkin, P. *Infrared and Raman Spectroscopy: Principles and Spectral Interpretation*; Elsevier: Amsterdam ; Boston, 2011.

(6) *Emerging Raman Applications and Techniques in Biomedical and Pharmaceutical Fields*; Morris, M. D., Matousek, P., Eds.; Biological and medical physics, biomedical engineering; Springer: Heidelburg ; New York, 2010.

(7) Li, Z.; Deen, M. J.; Kumar, S.; Selvaganapathy, P. R. Raman Spectroscopy for In-Line Water Quality Monitoring—Instrumentation and Potential. *Sensors* **2014**, *14* (9), 17275–17303.

(8) Ferraro, J. R.; Nakamoto, K.; Brown, C. W. Chapter 1 - Basic Theory. In *Introductory Raman Spectroscopy (Second Edition)*; Academic Press: San Diego, 2003; pp 1–94.

(9) Albrecht, A. C. On the Theory of Raman Intensities. *J. Chem. Phys.* **1961**, *34* (5), 1476–1484.

(10) Socrates, G. *Infrared and Raman Characteristic Group Frequencies: Tables and Charts*, 3. ed., repr. as paperback.; Wiley: Chichester, 2010.

(11) Dollish, F. R.; Fateley, W. G.; Bentley, F. F. *Characteristic Raman Frequencies of Organic Compounds*; Wiley, 1974.

(12) Lin-Vien, D.; Colthup, N. B.; Fateley, W. G.; Grasselli, J. G. *The Handbook of Infrared and Raman Characteristic Frequencies of Organic Molecules*; Elsevier, 1991.

(13) Nyquist, R. A.; Kagel, R. O. *Handbook of Infrared and Raman Spectra of Inorganic Compounds and Organic Salts: Infrared Spectra of Inorganic Compounds*; Academic Press, 2012.

(14) Weber, W. H.; Merlin, R. *Raman Scattering in Materials Science*; Springer Science & Business Media, 2013.

(15) Cantarero, A. Raman Scattering Applied to Materials Science. *Procedia Mater. Sci.* **2015**, *9*, 113–122.

(16) Peticolas, W. L. Applications of Raman Spectroscopy to Biological Macromolecules. *Biochimie* **1975**, *57* (4), 417–428.

(17) Rae, A.; Stosch, R.; Klapetek, P.; Hight Walker, A. R.; Roy, D. State of the Art Raman Techniques for Biological Applications. *Methods* **2014**, *68* (2), 338–347.

(18) Ayas, S.; Cinar, G.; Ozkan, A. D.; Soran, Z.; Ekiz, O.; Kocaay, D.; Tomak, A.; Toren, P.; Kaya, Y.; Tunc, I.; et al. Label-Free Nanometer-Resolution Imaging of Biological Architectures through Surface Enhanced Raman Scattering. *Sci. Rep.* **2013**, *3*.

(19) Smitthipong, W.; Gadiou, R.; Vidal, L.; Wagner, P.; Nardin, M. 3D Raman Images of Rubber Blends (IR–HNBR). *Vib. Spectrosc.* **2008**, *46* (1), 8–13.

(20) Furukawa, T.; Sato, H.; Murakami, R.; Zhang, J.; Noda, I.; Ochiai, S.; Ozaki, Y. Raman Microspectroscopy Study of Structure, Dispersibility, and Crystallinity of Poly(hydroxybutyrate)/poly(l-Lactic Acid) Blends. *Polymer* **2006**, *47* (9), 3132–3140.

(21) Tabaksblat, R.; Meier, R. J.; Kip, B. J. Confocal Raman Microspectroscopy: Theory and Application to Thin Polymer Samples. *Appl. Spectrosc.* **1992**, *46* (1), 60–68.

(22) Malard, L. M.; Pimenta, M. A.; Dresselhaus, G.; Dresselhaus, M. S. Raman Spectroscopy in Graphene. *Phys. Rep.* **2009**, *473* (5-6), 51–87.

(23) Gupta, A.; Chen, G.; Joshi, P.; Tadigadapa, S.; Eklund. Raman Scattering from High-Frequency Phonons in Supported N-Graphene Layer Films. *Nano Lett.* **2006**, *6* (12), 2667–2673.

(24) Ferrari, A. C.; Meyer, J. C.; Scardaci, V.; Casiraghi, C.; Lazzeri, M.; Mauri, F.; Piscanec, S.; Jiang, D.; Novoselov, K. S.; Roth, S.; et al. Raman Spectrum of Graphene and Graphene Layers. *Phys. Rev. Lett.* **2006**, *97* (18), 187401.

(25) Ni, Z. H.; Chen, W.; Fan, X. F.; Kuo, J. L.; Yu, T.; Wee, A. T. S.; Shen, Z. X. Raman Spectroscopy of Epitaxial Graphene on a SiC Substrate. *Phys. Rev. B* **2008**, *77* (11), 115416.

(26) Schmidt, D. A.; Ohta, T.; Beechem, T. E. Strain and Charge Carrier Coupling in Epitaxial Graphene. *Phys. Rev. B* **2011**, *84* (23), 235422.

(27) Yan, X.; Suzuki, T.; Kitahama, Y.; Sato, H.; Itoh, T.; Ozaki, Y. A Study on the Interaction of Single-Walled Carbon Nanotubes (SWCNTs) and Polystyrene (PS) at the Interface in SWCNT–PS Nanocomposites Using Tip-Enhanced Raman Spectroscopy. *Phys. Chem. Chem. Phys.* **2013**, *15* (47), 20618–20624.

(28) Suzuki, T.; Itoh, T.; Vantasin, S.; Minami, S.; Kutsuma, Y.; Ashida, K.; Kaneko, T.; Morisawa, Y.; Miura, T.; Ozaki, Y. Tip-Enhanced Raman Spectroscopic Measurement of Stress Change in the Local Domain of Epitaxial Graphene on the Carbon Face of 4H-SiC(0001¯). *Phys. Chem. Chem. Phys.* **2014**, *16* (37), 20236–20240.

(29) Booth, M. J. Adaptive Optical Microscopy: The Ongoing Quest for a Perfect Image. *Light Sci. Appl.* **2014**, *3* (4), e165.

(30) Weisenburger, S.; Sandoghdar, V. Light Microscopy: An Ongoing Contemporary Revolution. *Contemp. Phys.* **2015**, *56* (2), 123–143.

(31) Heintzmann, R.; Ficz, G. Breaking the Resolution Limit in Light Microscopy. *Brief. Funct. Genomic. Proteomic.* **2006**, *5* (4), 289–301.

(32) Freitag, B.; Kujawa, S.; Mul, P. M.; Ringnalda, J.; Tiemeijer, P. C. Breaking the Spherical and Chromatic Aberration Barrier in Transmission Electron Microscopy. *Ultramicroscopy* **2005**, *102* (3), 209–214.

(33) Yu, J.; Saito, Y.; Ichimura, T.; Kawata, S.; Verma, P. Far-Field Free Tapping-Mode Tip-Enhanced Raman Microscopy. *Appl. Phys. Lett.* **2013**, *102* (12), 123110.

(34) Saito, Y.; Verma, P.; Masui, K.; Inouye, Y.; Kawata, S. Nano-Scale Analysis of Graphene Layers by Tip-Enhanced near-Field Raman Spectroscopy. *J. Raman Spectrosc.* **2009**, *40* (10), 1434–1440.

(35) Poborchii, V.; Tada, T.; Kanayama, T. Study of Stress in a Shallow-Trench-Isolated Si Structure Using Polarized Confocal near-UV Raman Microscopy of Its Cross Section. *Appl. Phys. Lett.* **2007**, *91* (24), 241902.

(36) Tisinger, L. G.; Sommer, A. J. Attenuated Total Internal Reflection (ATR) Raman Microspectroscopy. *Microsc. Microanal.* **2004**, *null* (Supplement S02), 1318–1319.

(37) Asher, S. A. Ultraviolet Raman Spectrometry. In *Handbook of Vibrational Spectroscopy*; John Wiley & Sons, Ltd, 2006.

(38) Zheng, X.; Zong, C.; Xu, M.; Wang, X.; Ren, B. Raman Imaging from Microscopy to Nanoscopy, and to Macroscopy. *Small* **2015**, *11* (28), 3395–3406.

(39) Kasim, J.; Ting, Y.; Meng, Y. Y.; Ping, L. J.; See, A.; Jong, L. L.; Xiang, S. Z. Near-Field Raman Imaging Using Optically Trapped Dielectric Microsphere. *Opt. Express* **2008**, *16* (11), 7976–7984.

(40) Lereu, A. l.; Passian, A.; Dumas, P. Near Field Optical Microscopy: A Brief Review. *Int. J. Nanotechnol.* **2012**, *9* (3-7), 488–501.

(41) Saiki, T. Recent Advances in near-Field Optical Microscopy. In *Microprocesses and Nanotechnology Conference, 2002. Digest of Papers. Microprocesses and Nanotechnology 2002. 2002 International*; 2002; pp 6–7.

(42) Futamata, M.; Bruckbauer, A. ATR-SNOM-Raman Spectroscopy. *Chem. Phys. Lett.* **2001**, *341* (5–6), 425–430.

(43) Jahncke, C. L.; Paesler, M. A.; Hallen, H. D. Raman Imaging with Near-field Scanning Optical Microscopy. *Appl. Phys. Lett.* **1995**, *67* (17), 2483–2485.

(44) Gouadec, G.; Colomban, P. Raman Spectroscopy of Nanomaterials: How Spectra Relate to Disorder, Particle Size and Mechanical Properties. *Prog. Cryst. Growth Charact. Mater.* **2007**, *53* (1), 1–56.

(45) Schaller, R. D.; Ziegelbauer, J.; Lee, L. F.; Haber, L. H.; Saykally, R. J. Chemically Selective Imaging of Subcellular Structure in Human Hepatocytes with Coherent Anti-Stokes Raman Scattering (CARS) Near-Field Scanning Optical Microscopy (NSOM). *J. Phys. Chem. B* **2002**, *106* (34), 8489–8492.

(46) Kaupp, G. Scanning near-Field Optical Microscopy on Rough Surfaces: Applications in Chemistry, Biology, and Medicine. *Int. J. Photoenergy* **2006**, *2006*, e69878.

(47) Webster, S.; Smith, D. A.; Batchelder, D. N. Raman Microscopy Using a Scanning near-Field Optical Probe. *Vib. Spectrosc.* **1998**, *18* (1), 51–59.

(48) Goetz, M.; Drews, D.; Zahn, D. R. T.; Wannemacher, R. Near-Field Raman Spectroscopy of Semiconductor Heterostructures and CVD-Diamond Layers. *J. Lumin.* **1998**, *76–77*, 306–309.

(49) Grosse, K. Nanometer-Scale Temperature Measurements of Phase Change Memory and Carbon Nanomaterials, University of Illinois: Urbana, Illinois, 2014.

(50) Willets, K. A.; Duyne, R. P. V. Localized Surface Plasmon Resonance Spectroscopy and Sensing. *Annu. Rev. Phys. Chem.* **2007**, *58* (1), 267–297.

(51) Richards, D.; Milner, R. G.; Huang, F.; Festy, F. Tip-Enhanced Raman Microscopy: Practicalities and Limitations. *J. Raman Spectrosc.* **2003**, *34* (9), 663–667.

(52) Douillard, L.; Charra, F.; Korczak, Z.; Bachelot, R.; Kostcheev, S.; Lerondel, G.; Adam, P.-M.; Royer, P. Short Range Plasmon Resonators Probed by Photoemission Electron Microscopy. *Nano Lett.* **2008**, *8* (3), 935–940.

(53) Kawata, S.; Inouye, Y.; Verma, P. Plasmonics for near-Field Nano-Imaging and Superlensing. *Nat. Photonics* **2009**, *3* (7), 388–394.

(54) Chen, C.; Hayazawa, N.; Kawata, S. A 1.7 Nm Resolution Chemical Analysis of Carbon Nanotubes by Tip-Enhanced Raman Imaging in the Ambient. *Nat. Commun.* **2014**, *5*, 3312.

(55) Ichimura, T.; Fujii, S.; Verma, P.; Yano, T.; Inouye, Y.; Kawata, S. Subnanometric Near-Field Raman Investigation in the Vicinity of a Metallic Nanostructure. *Phys. Rev. Lett.* **2009**, *102* (18), 186101.

(56) Yano, T.; Verma, P.; Saito, Y.; Ichimura, T.; Kawata, S. Pressure-Assisted Tip-Enhanced Raman Imaging at a Resolution of a Few Nanometres. *Nat. Photonics* **2009**, *3* (8), 473–477.

(57) Zhang, R.; Zhang, Y.; Dong, Z. C.; Jiang, S.; Zhang, C.; Chen, L. G.; Zhang, L.; Liao, Y.; Aizpurua, J.; Luo, Y.; et al. Chemical Mapping of a Single Molecule by Plasmon-Enhanced Raman Scattering. *Nature* **2013**, *498* (7452), 82–86.

(58) Pettinger, B. Single-Molecule Surface- and Tip-Enhanced Raman Spectroscopy. *Mol. Phys.* **2010**, *108* (16), 2039–2059.

(59) Cvitkovic, A.; Ocelic, N.; Hillenbrand, R. Material-Specific Infrared Recognition of Single Sub-10 Nm Particles by Substrate-Enhanced Scattering-Type Near-Field Microscopy. *Nano Lett.* **2007**, *7* (10), 3177–3181.

(60) Hillenbrand, R.; Keilmann, F. Material-Specific Mapping of Metal/semiconductor/dielectric Nanosystems at 10 Nm Resolution by Backscattering near-Field Optical Microscopy. *Appl. Phys. Lett.* **2002**, *80* (1), 25–27.

(61) Ji, W.; Spegazzini, N.; Kitahama, Y.; Chen, Y.; Zhao, B.; Ozaki, Y. pH-Response Mechanism of P-Aminobenzenethiol on Ag Nanoparticles Revealed By Two-Dimensional Correlation Surface-Enhanced Raman Scattering Spectroscopy. *J. Phys. Chem. Lett.* **2012**, *3* (21), 3204–3209.

(62) Yang, S.; Dai, X.; Stogin, B. B.; Wong, T.-S. Ultrasensitive Surface-Enhanced Raman Scattering Detection in Common Fluids. *Proc. Natl. Acad. Sci.* **2016**, *113* (2), 268–273.

(63) He, X.; Wang, H.; Li, Z.; Chen, D.; Liu, J.; Zhang, Q. Ultrasensitive SERS Detection of Trinitrotoluene through Capillarity-Constructed Reversible Hot Spots Based on ZnO–Ag Nanorod Hybrids. *Nanoscale* **2015**, *7* (18), 8619–8626.

(64) Fan, Z.; Kanchanapally, R.; Ray, P. C. Hybrid Graphene Oxide Based Ultrasensitive SERS Probe for Label-Free Biosensing. *J. Phys. Chem. Lett.* **2013**, *4* (21), 3813–3818.

(65) Xu, L.; Yin, H.; Ma, W.; Kuang, H.; Wang, L.; Xu, C. Ultrasensitive SERS Detection of Mercury Based on the Assembled Gold Nanochains. *Biosens. Bioelectron.* **2015**, *67*, 472–476.

(66) Zhao, S.; Ma, W.; Xu, L.; Wu, X.; Kuang, H.; Wang, L.; Xu, C. Ultrasensitive SERS Detection of VEGF Based on a Self-Assembled Ag ornamented–AU Pyramid Superstructure. *Biosens. Bioelectron.* **2015**, *68*, 593–597.

(67) *Surface-Enhanced Raman Scattering*; Kneipp, K., Moskovits, M., Kneipp, H., Eds.; Topics in Applied Physics; Springer Berlin Heidelberg, 2006; Vol. 103.

(68) McQuillan, A. J. The Discovery of Surface-Enhanced Raman Scattering. *Notes Rec. R. Soc.* **2009**, *63* (1), 105–109.

(69) Jeanmaire, D. L.; Van Duyne, R. P. Surface Raman Spectroelectrochemistry. *J. Electroanal. Chem. Interfacial Electrochem.* **1977**, *84* (1), 1–20.

(70) Albrecht, M. G.; Creighton, J. A. Anomalously Intense Raman Spectra of Pyridine at a Silver Electrode. *J. Am. Chem. Soc.* **1977**, *99* (15), 5215–5217.

(71) Burstein, E.; Chen, Y. J.; Chen, C. Y.; Lundquist, S.; Tosatti, E. “Giant” Raman Scattering by Adsorbed Molecules on Metal Surfaces. *Solid State Commun.* **1979**, *29* (8), 567–570.

(72) Persson, B. N. J. On the Theory of Surface-Enhanced Raman Scattering. *Chem. Phys. Lett.* **1981**, *82* (3), 561–565.

(73) Gersten, J. I.; Birke, R. L.; Lombardi, J. R. Theory of Enhance I Light Scattering from Molecules Adsorbed at the Metal-Solution Interface. *Phys. Rev. Lett.* **1979**, *43* (2), 147–150.

(74) Lombardi, J. R.; Birke, R. L.; Lu, T.; Xu, J. Charge-transfer Theory of Surface Enhanced Raman Spectroscopy: Herzberg–Teller Contributions. *J. Chem. Phys.* **1986**, *84* (8), 4174–4180.

(75) Lombardi, J. R.; Birke, R. L. Theory of Surface-Enhanced Raman Scattering in Semiconductors. *J. Phys. Chem. C* **2014**, *118* (20), 11120–11130.

(76) Le Ru, E. C.; Etchegoin, P. G. *Principles of Surface-Enhanced Raman Spectroscopy: And Related Plasmonic Effects*, 1st ed.; Elsevier: Amsterdam ; Boston, 2009.

(77) *Surface Plasmon Nanophotonics*; Brongersma, M. L., Kik, P. G., Eds.; Springer series in optical

sciences; Springer: Dordrecht, 2007.

(78) Huang, K.-C.; Bando, K.; Ando, J.; Smith, N. I.; Fujita, K.; Kawata, S. 3D SERS (surface Enhanced Raman Scattering) Imaging of Intracellular Pathways. *Methods* **2014**, *68* (2), 348–353.

(79) Asghari-Khiavi, M.; Wood, B. R.; Hojati-Talemi, P.; Downes, A.; McNaughton, D.; Mechler, A. Exploring the Origin of Tip-Enhanced Raman Scattering; Preparation of Efficient TERS Probes with High Yield. *J. Raman Spectrosc.* **2012**, *43* (2), 173–180.

(80) Taguchi, A.; Yu, J.; Verma, P.; Kawata, S. Optical Antennas with Multiple Plasmonic Nanoparticles for Tip-Enhanced Raman Microscopy. *Nanoscale* **2015**, *7* (41), 17424–17433.

(81) Schuck, P. J.; Weber-Bargioni, A.; Ashby, P. D.; Ogletree, D. F.; Schwartzberg, A.; Cabrini, S. Life Beyond Diffraction: Opening New Routes to Materials Characterization with Next-Generation Optical Near-Field Approaches. *Adv. Funct. Mater.* **2013**, *23* (20), 2539–2553.

(82) Kumar, N.; Stephanidis, B.; Zenobi, R.; Wain, A. J.; Roy, D. Nanoscale Mapping of Catalytic Activity Using Tip-Enhanced Raman Spectroscopy. *Nanoscale* **2015**, *7* (16), 7133–7137.

(83) Wang, X.; Liu, Z.; Zhuang, M.-D.; Zhang, H.-M.; Wang, X.; Xie, Z.-X.; Wu, D.-Y.; Ren, B.; Tian, Z.-Q. Tip-Enhanced Raman Spectroscopy for Investigating Adsorbed Species on a Single-Crystal Surface Using Electrochemically Prepared Au Tips. *Appl. Phys. Lett.* **2007**, *91* (10), 101105.

(84) Tarun, A.; Hayazawa, N.; Kawata, S. Tip-Enhanced Raman Spectroscopy for Nanoscale Strain Characterization. *Anal. Bioanal. Chem.* **2009**, *394* (7), 1775–1785.

(85) Suzuki, T.; Yan, X.; Kitahama, Y.; Sato, H.; Itoh, T.; Miura, T.; Ozaki, Y. Tip-Enhanced Raman Spectroscopy Study of Local Interactions at the Interface of Styrene–Butadiene Rubber/Multiwalled Carbon Nanotube Nanocomposites. *J. Phys. Chem. C* **2013**, *117* (3), 1436–1440.

(86) Kawata, S.; Verma, P. Optical Nano-Imaging of Materials: Peeping Through Tip-Enhanced Raman Scattering. *Chim. Int. J. Chem.* **2006**, *60* (11), 770–776.

(87) Yano, T.; Ichimura, T.; Kuwahara, S.; H'Dhili, F.; Uetsuki, K.; Okuno, Y.; Verma, P.; Kawata, S. Tip-Enhanced Nano-Raman Analytical Imaging of Locally Induced Strain Distribution in Carbon Nanotubes. *Nat. Commun.* **2013**, *4*.

(88) Chaunchaiyakul, S.; Yano, T.; Khoklang, K.; Krukowski, P.; Akai-Kasaya, M.; Saito, A.; Kuwahara, Y. Nanoscale Analysis of Multiwalled Carbon Nanotube by Tip-Enhanced Raman Spectroscopy. *Carbon* **2016**, *99*, 642–648.

(89) Xu, G.; Liu, Z.; Xu, K.; Zhang, Y.; Zhong, H.; Fan, Y.; Huang, Z. Constant Current Etching of Gold Tips Suitable for Tip-Enhanced Raman Spectroscopy. *Rev. Sci. Instrum.* **2012**, *83* (10), 103708.

(90) Poliani, E.; Nippert, F.; Maultzsch, J. Effect of Gap Modes on Graphene and Multilayer Graphene in Tip-Enhanced Raman Spectroscopy. *Phys. Status Solidi B* **2012**, *249* (12), 2511–2514.

(91) Rickman, R. H.; Dunstan, P. R. Enhancement of Lattice Defect Signatures in Graphene and Ultrathin Graphite Using Tip-Enhanced Raman Spectroscopy: Enhancement of Defect Signatures in Graphene Using Tip-Enhanced Raman. *J. Raman Spectrosc.* **2014**, *45* (1), 15–21.

(92) Hoffmann, G. G.; Xue, L.; Loos, J.; de With, G. High-Resolution Tip-Enhanced Raman Mapping. *Macromol. Symp.* **2011**, *305* (1), 26–42.

(93) Hoffmann, G. G.; de With, G.; Loos, J. Micro-Raman and Tip-Enhanced Raman Spectroscopy of Carbon Allotropes. *Macromol. Symp.* **2008**, *265* (1), 1–11.

(94) Snitka, V.; Rodrigues, R. D.; Lendraitis, V. Novel Gold Cantilever for Nano-Raman Spectroscopy of Graphene. *Microelectron. Eng.* **2011**, *88* (8), 2759–2762.

(95) Wang, P.; Zhang, D.; Li, L.; Li, Z.; Zhang, L.; Fang, Y. Reversible Defect in Graphene Investigated by Tip-Enhanced Raman Spectroscopy. *Plasmonics* **2012**, *7* (3), 555–561.

(96) Ghislandi, M.; Hoffmann, G. G.; Tkalya, E.; Xue, L.; With, G. D. Tip-Enhanced Raman Spectroscopy and Mapping of Graphene Sheets. *Appl. Spectrosc. Rev.* **2012**, *47* (5), 371–381.

(97) Domke, K. F.; Pettinger, B. Tip-Enhanced Raman Spectroscopy of 6H-SiC with Graphene Adlayers: Selective Suppression of E1 Modes. *J. Raman Spectrosc.* **2009**, *40* (10), 1427–1433.

(98) Pashaee, F.; Sharifi, F.; Fanchini, G.; Lagugné-Labarthet, F. Tip-Enhanced Raman Spectroscopy of Graphene-like and Graphitic Platelets on Ultraflat Gold Nanoplates. *Phys. Chem. Chem. Phys.* **2015**, *17* (33), 21315–21322.

(99) Shiotari, A.; Kumagai, T.; Wolf, M. Tip-Enhanced Raman Spectroscopy of Graphene Nanoribbons on Au(111). *J. Phys. Chem. C* **2014**, *118* (22), 11806–11812.

(100) Su, W.; Roy, D. Visualizing Graphene Edges Using Tip-Enhanced Raman Spectroscopy. *J. Vac. Sci. Technol. B* **2013**, *31* (4), 041808.

(101) Klingsporn, J. M.; Jiang, N.; Pozzi, E. A.; Sonntag, M. D.; Chulhai, D.; Seideman, T.; Jensen, L.; Hersam, M. C.; Duyne, R. P. V. Intramolecular Insight into Adsorbate–Substrate Interactions via Low-Temperature, Ultrahigh-Vacuum Tip-Enhanced Raman Spectroscopy. *J. Am. Chem. Soc.* **2014**, *136* (10), 3881–3887.

(102) Berweger, S.; Atkin, J. M.; Olmon, R. L.; Raschke, M. B. Light on the Tip of a Needle: Plasmonic

Nanofocusing for Spectroscopy on the Nanoscale. *J. Phys. Chem. Lett.* **2012**, *3* (7), 945–952.

(103) Zeng, Z.-C.; Huang, S.-C.; Li, M.-H.; Huang, T.; Ren, B. Electrochemical Tip-Enhanced Raman Spectroscopy (EC-TERS). *Meet. Abstr.* **2014**, *MA2014-03* (4), 497–497.

(104) Zeng, Z.-C.; Huang, S.-C.; Wu, D.-Y.; Meng, L.-Y.; Li, M.-H.; Huang, T.-X.; Zhong, J.-H.; Wang, X.; Yang, Z.-L.; Ren, B. Electrochemical Tip-Enhanced Raman Spectroscopy. *J. Am. Chem. Soc.* **2015**, *137* (37), 11928–11931.

(105) Gui, G.; Li, J.; Zhong, J. Band Structure Engineering of Graphene by Strain: First-Principles Calculations. *Phys. Rev. B* **2008**, *78* (7), 075435.

(106) Duplock, E. J.; Scheffler, M.; Lindan, P. J. D. Hallmark of Perfect Graphene. *Phys. Rev. Lett.* **2004**, *92* (22), 225502.

(107) Low, T.; Guinea, F.; Katsnelson, M. I. Gaps Tunable by Electrostatic Gates in Strained Graphene. *Phys. Rev. B* **2011**, *83* (19), 195436.

(108) Ni, Z. H.; Yu, T.; Lu, Y. H.; Wang, Y. Y.; Feng, Y. P.; Shen, Z. X. Uniaxial Strain on Graphene: Raman Spectroscopy Study and Band-Gap Opening. *ACS Nano* **2008**, *2* (11), 2301–2305.

(109) Jiang, Z.; Zhang, Y.; Tan, Y.-W.; Stormer, H. L.; Kim, P. Quantum Hall Effect in Graphene. *Solid State Commun.* **2007**, *143* (1–2), 14–19.

(110) Jobst, J.; Waldmann, D.; Speck, F.; Hirner, R.; Maude, D. K.; Seyller, T.; Weber, H. B. Quantum Oscillations and Quantum Hall Effect in Epitaxial Graphene. *Phys. Rev. B* **2010**, *81* (19), 195434.

(111) Novoselov, K. S.; Geim, A. K.; Morozov, S. V.; Jiang, D.; Zhang, Y.; Dubonos, S. V.; Grigorieva, I. V.; Firsov, A. A. Electric Field Effect in Atomically Thin Carbon Films. *Science* **2004**, *306* (5696), 666–669.

(112) Lee, C.; Wei, X.; Kysar, J. W.; Hone, J. Measurement of the Elastic Properties and Intrinsic Strength of Monolayer Graphene. *Science* **2008**, *321* (5887), 385–388.

(113) Ling, X.; Xie, L.; Fang, Y.; Xu, H.; Zhang, H.; Kong, J.; Dresselhaus, M. S.; Zhang, J.; Liu, Z. Can Graphene Be Used as a Substrate for Raman Enhancement? *Nano Lett.* **2010**, *10* (2), 553–561.

(114) Ling, X.; Moura, L. G.; Pimenta, M. A.; Zhang, J. Charge-Transfer Mechanism in Graphene-Enhanced Raman Scattering. *J. Phys. Chem. C* **2012**, *116* (47), 25112–25118.

(115) Xu, W.; Mao, N.; Zhang, J. Graphene: A Platform for Surface-Enhanced Raman Spectroscopy. *Small* **2013**, *9* (8), 1206–1224.

(116) Allen, M. J.; Tung, V. C.; Kaner, R. B. Honeycomb Carbon: A Review of Graphene. *Chem. Rev.* **2010**, *110* (1), 132–145.

(117) Blake, P.; Hill, E. W.; Castro Neto, A. H.; Novoselov, K. S.; Jiang, D.; Yang, R.; Booth, T. J.; Geim, A. K. Making Graphene Visible. *Appl. Phys. Lett.* **2007**, *91* (6), 063124.

(118) Xia, F.; Mueller, T.; Lin, Y.; Valdes-Garcia, A.; Avouris, P. Ultrafast Graphene Photodetector. *Nat. Immunol.* **2009**, *4* (12), 839–843.

(119) Lin, Y.-M.; Dimitrakopoulos, C.; Jenkins, K. A.; Farmer, D. B.; Chiu, H.-Y.; Grill, A.; Avouris, P. 100-GHz Transistors from Wafer-Scale Epitaxial Graphene. *Science* **2010**, *327* (5966), 662–662.

(120) Liu, C.; Yu, Z.; Neff, D.; Zhamu, A.; Jang, B. Z. Graphene-Based Supercapacitor with an Ultrahigh Energy Density. *Nano Lett.* **2010**, *10* (12), 4863–4868.

(121) Wang, Y.; Shi, Z.; Huang, Y.; Ma, Y.; Wang, C.; Chen, M.; Chen, Y. Supercapacitor Devices Based on Graphene Materials. *J. Phys. Chem. C* **2009**, *113* (30), 13103–13107.

(122) Le, L. T.; Ervin, M. H.; Qiu, H.; Fuchs, B. E.; Lee, W. Y. Graphene Supercapacitor Electrodes Fabricated by Inkjet Printing and Thermal Reduction of Graphene Oxide. *Electrochem. Commun.* **2011**, *13* (4), 355–358.

(123) Das, A.; Pisana, S.; Chakraborty, B.; Piscanec, S.; Saha, S. K.; Waghmare, U. V.; Novoselov, K. S.; Krishnamurthy, H. R.; Geim, A. K.; Ferrari, A. C.; et al. Monitoring Dopants by Raman Scattering in an Electrochemically Top-Gated Graphene Transistor. *Nat. Nanotechnol.* **2008**, *3* (4), 210–215.

(124) Stankovich, S.; Dikin, D. A.; Piner, R. D.; Kohlhaas, K. A.; Kleinhammes, A.; Jia, Y.; Wu, Y.; Nguyen, S. T.; Ruoff, R. S. Synthesis of Graphene-Based Nanosheets via Chemical Reduction of Exfoliated Graphite Oxide. *Carbon* **2007**, *45* (7), 1558–1565.

(125) McAllister, M. J.; Li, J.-L.; Adamson, D. H.; Schniepp, H. C.; Abdala, A. A.; Liu, J.; Herrera-Alonso, M.; Milius, D. L.; Car, R.; Prud'homme, R. K.; et al. Single Sheet Functionalized Graphene by Oxidation and Thermal Expansion of Graphite. *Chem. Mater.* **2007**, *19* (18), 4396–4404.

(126) Zhou, Y.; Bao, Q.; Tang, L. A. L.; Zhong, Y.; Loh, K. P. Hydrothermal Dehydration for the "Green" Reduction of Exfoliated Graphene Oxide to Graphene and Demonstration of Tunable Optical Limiting Properties. *Chem. Mater.* **2009**, *21* (13), 2950–2956.

(127) Stadler, J.; Schmid, T.; Zenobi, R. Nanoscale Chemical Imaging of Single-Layer Graphene. *ACS Nano* **2011**, *5* (10), 8442–8448.

Chapter I: Tip-Enhanced Raman Scattering of the Local Nanostructure of Epitaxial Graphene Grown on 4H-SiC $(000\overline{1})$

Abstract

Step, ridge, and crack sub-micro/nanostructures of epitaxial graphene on 4H-SiC $(000\bar{1})$ were characterized using tip-enhanced Raman scattering (TERS) spectroscopy. The nanostructures were created during graphene synthesis due to a difference in the thermal expansion coefficient of graphene and SiC. These structures are a distinctive property of epitaxial graphene, together with other desirable properties, such as large graphene sheet and minimal defects. The results of this study illustrate that the exceptional spatial resolution of TERS allows spectroscopic measurements of individual nanostructures, a feat which normal Raman spectroscopy is not capable of. By analyzing TERS spectra, the change of local strain on the nanoridge and decreased graphene content in the sub-micrometer crack were detected. Using G' band positions in the TERS spectra, the strain difference between ridge center and flat area was calculated to be 1.6×10^{-3} and 5.8×10^{-4} for uniaxial and biaxial strain, respectively. This confirms the proposed mechanism in previous researches that nanoridges on epitaxial graphene form as a relief against compressive strain. With this study, we demonstrate that TERS is a powerful technique for the characterization of individual local nanostructures on epitaxial graphene.

Introduction

Graphene is considered as a future material for chemical sensors, biosensors, and electronic devices due to its outstanding properties including, but not limited to, tremendous carrier mobility and a unique band gap.[1–4] Among various types of graphene, epitaxial graphene grown on SiC has garnered considerable attention because of its large sheet area, minimal defects, and the electrical insulation properties of SiC, which allow the application in electronic circuits without the need of substrate transfer processes.[5,6] The transparency of SiC under visible light can also be advantageous in graphene-based opto-electronic device.[7] Graphene grown on either face of SiC does have differing properties: while graphene grown on Si face (0001 face) of SiC attaches strongly to the SiC surface, graphene grown on the C-face ($000\bar{1}$ face) has a weaker attraction to the SiC substrate due to the presence a carbon buffer layer.[8] This allows some unique features of graphene on C face to occur, such as stack disordering of multilayer graphene, which allows extremely high mobility and unique nanostructures on the graphene sheet, which alters physical and electronic properties.[9] It has been known that nanostructures can affect band gap[10], electron mobility[11], and internal strain[12] of graphene. Therefore, it is possible to use strain engineering to control and manipulate the nanostructures and produce interesting products such as large band gap graphene.[13]

To characterize nanostructures of graphene grown on C-face and understand their forming mechanism, many groups have used atomic force microscopy (AFM)[12], scanning tunneling microscope (STM)[11,14,15], and angle-resolved photoemission spectroscopy (ARPES)[16] to study the morphology, occurrence frequency, synthesis temperature dependence, and effects on band structure of the most common nanostructures, e.g. ridges and steps. Among several techniques, Raman spectroscopy is considered as an ideal technique for graphene characterization because it provides robust information about defects[17–21], internal strain[22–26], stacking configuration[27,28], number of layers[27,29–32], and doping[7,24,33]. There are some publications about using Raman spectroscopy to characterize nanostructures on epitaxial graphene with insightful results, e.g. occurrences of defect in some types of nanostructures.[9,34,35] However, the spatial resolution of normal Raman spectroscopy is limited by the diffraction of light, generally no better than a few hundred nanometers. Meanwhile, sizes of nanostructures and distances between them can be smaller than one hundreds nanometers.[34,35] Therefore, Raman signals in those studies came from domains of nanostructures rather than individual structure, and the effects of individual nanostructures on the properties of graphene still have not been deeply investigated.

Tip-enhanced Raman scattering (TERS) spectroscopy is a technique that employs near-field enhancement from a metallic nanotip to obtain Raman spectra with spatial resolution surpassing the diffraction limit.[36–41] To achieve a good enhancement, the size, shape, and material of the tips must be carefully chosen to ensure plasmon resonance with the excitation laser light.[42,43] The evanescent field from this resonance is confined to a small area around the tip, resulting in the improvement of spatial resolution.[36] This characteristic of TERS is very useful in graphene studies.[30] Saito et al., Hoffmann et al., and Ghislandi et al. used TERS to determine number of layers on exfoliated and CVD graphene with nano-scale resolution.[30–32] Stadler et al. demonstrated the capability of TERS in the detection of chemical contamination on CVD graphene.[17] Furthermore, some other groups explored lattice defects, edge defects, and gap mode of exfoliated graphene with a remarkable resolution using TERS.[44–47] TERS spectra of epitaxial graphene on 6H–SiC also show selective suppression of SiC E1 mode.[42] In our previous paper, we found a nano-scale position dependence of strain in epitaxial graphene by using TERS.[48] Nevertheless, to the best of our knowledge, there are still no published reports about the quantitative analysis of strain using TERS on nanostructures of epitaxial graphene. In this study, we correlate TERS spectra from epitaxial graphene nanostructures to the corresponding AFM topology and demonstrate that TERS is an excellent technique for characterization of nanostructures on C-face grown epitaxial graphene. With the spatial resolution better than one hundred nanometers, the Raman spectrum of each graphene nanostructure can be acquired individually. With this capability, we can use TERS to quantitatively measure the effect of ridge structure on strain. We also found that TERS can detect the absence of graphene in small crack structure that normal Raman spectroscopy cannot.

Experimental Section

Epitaxial graphene was synthesized by annealing 4H-SiC $(000\bar{1})$ in ultrahigh vacuum at 1800 °C for 15 minutes using semi-closed TaC containers. The sublimation of Si from SiC was regulated by an adjustment of Si vapor pressure inside the container, resulting in precise control of graphene growth rate, number of layers, and domain size. The synthesis details are well-documented in our previous paper.[5]

TERS spectra were measured by Photon Design Nanostar NFRSM800 with the 514.5 nm line of an argon ion laser (Spectra Physics Stabilite 2017) as an excitation source. The setup was top-illumination and top-collection using the same objective lens (×90 magnification, 0.71 NA). For each TERS measurement, the spectra were acquired in a tip-attached position and then in a tip-retracted position. The tip-attached spectrum was subtracted by tip-retracted spectrum to provide the TERS spectrum. When signal from the far-field component is subtracted out, the TERS spectrum solely represents the near-field component (signal from the small area around the tip). Surface topology was acquired by non-contact mode AFM (UNISOKU Co. LTD) with 45° angle between tip and sample surface. The AFM tips (UNISOKU Co. LTD) were silver bulk tips made by electrochemical etching process with ~75 nm tip radius. The estimated tip-sample separation in the non-contact mode was < 1 nm, according to the manufacturer. Calibration procedure of Z-axis piezoelectric element was done using standard grating with 90 nm depth structure.

Results and discussion

TERS spectra of epitaxial graphene

Tip-attached, tip-retracted, and subtracted (TERS) spectra of single-layer epitaxial graphene on the C-face of SiC are shown in Figure 1. Band assignments are summarized in Table 1. One of the two most prominent peaks, the G band, is the only band of graphene that originates from normal first-order Raman scattering. This band arises from a doubly degenerate in-plane transverse optical phonon (iTO phonon) and a longitudinal phonon (LO phonon) around the Γ point in the first Brillouin zone. Another intense peak, the G' band (also called the 2D band), is contributed by a double resonance process of two iTO phonons around the K point.[27] The spectra in Figure 1 give typical features of single layer graphene such as a high intensity ratio between the G'/G bands (> 1) and a small FWHM of the G' band (~23 cm^{-1}). Note that not every area in this sample provides the spectrum of single layer graphene, which is correlated with a sample average of 1.7 layers measured using visible light absorption. The D band (~1350 cm^{-1}), which emerges from the double resonance process of defects and iTO phonons around the K point,[27] is absent in the spectra, indicating high quality graphene sheet with minimal defects. By considering the ratio of probe areas between TERS and far-field Raman spectroscopy (1:180), the enhancement factor in Figure 1 can be evaluated to be ~55 for graphene G' band and ~32 for SiC E_2 band. Nevertheless, the enhancement factor is greatly dependent on the tip quality. We recently reported an enhancement factor up to 1000 using the same instrument and a similar sample.[48] The larger enhancement in graphene bands compared to SiC bands is due to the influence of the carbon buffer layer on the C-face ($000\bar{1}$ face) of SiC. The effect of buffer layer on the difference in enhancement factor was discussed in our previous paper.[48]

Table 1. Band assignments for the spectra in Figure 1.

Raman shift (cm^{-1})	assignments[27,49,50]
776	SiC E_2 (TO)
982	SiC A_1 (LO)
1528	SiC (optical branch)
1590	graphene G band (E_{2g} LO, iTO)
1692,1710	SiC (optical branch)
2459	graphene G* band (LA + iTO)
2708	graphene G' band (iTO + iTO)
3249	graphene 2D' band (LO + LO)

TERS spectra of step and ridge nanostructures

The epitaxial graphene forms patch-like areas throughout the sample. Data from AFM topology suggests that most areas are very flat (a few nanometers in height variation). However, in some areas, the epitaxial graphene shows unusual features that are not found in graphene from mechanical cleavage; for example, a step nanostructure is shown in Figure 2a. This step is about 2 nm high and originates from the step-terrace structure initially present on the SiC substrate. Figure 2b shows the G' band region of far-field Raman (tip retracted) and TERS (tip attached minus tip retracted) spectra obtained from five points across the step shown in Figure 2a. They all provide high $I_G/I_{G'}$ ratios (> 1) and small FWHM of G' band (18

– 23 cm^{-1}), which are characteristics of single-layer graphene. Although twisted double-layer graphene with G and G' bands similar to single layer graphene is commonly seen on epitaxial graphene,[51] our Raman spectra do not show the characteristic I band (~1375 cm^{-1}) of twisted double layers.[28] This confirms that the step structure does not arise from a difference in the number of graphene layers, but rather from the inherent structure of the substrate. This structure, however, does not affect the G' band position significantly in both far-field Raman and TERS spectra (Figure 2c). The absence of a phonon frequency change implies that there is no significant strain difference between graphene on either side of the step.

A different nanostructure, on the contrary, alters the strain and causes the position of the G' band to change. Figure 3a depicts an AFM image of a ridge nanostructure. This ridge is the result of a difference in thermal expansion coefficients between graphene (measured: -1×10^{-6} K^{-1} @ 300 K, calculated: negative throughout 0–2000 K) and the SiC substrate (4.5×10^{-6} K^{-1}).[52,53] Upon cooling from the synthesizing temperature, SiC shrank faster than graphene. Thus, the graphene sheet experienced compression. When the compressive strain is greater than critical buckling strain, some parts of the graphene sheet are pushed out of the plane to form a ridge.[54] This compression-induced ridge-forming mechanism is well-explained in many papers.[11,12,14,15] The AFM topology image in Figure 3a shows the ridge to have a ~6 nm height and a ~ 150 nm width. Far-field Raman and TERS spectra shown in Figure 3b were obtained from seven points across the ridge. Since the points are not exactly on a straight line, the distances shown in Figure 3c, 3d, and 3e were measured using the point on the line nearest to each measurement point. Every TERS and far-field Raman spectrum in this area exhibits the G' band FWHM and $I_G/I_{G'}$ ratio of single-layer graphene. For the points on the ridge, the graphene G' bands in the TERS spectra (Figure 3b) have lower Raman shifts compared to bands in far-field spectra. The plot of peak position from Lorentzian fitting in Figure 3c clearly demonstrates the capability of improved spatial resolution with TERS. In TERS spectra, the G' band shows a Raman shift reduced by 8.7 cm^{-1} on the ridge compared to the flat area. Since the tip was controlled by non-contact mode AFM, the spectral change is certainly not from a deformation caused by the tip. Therefore, the lower Raman shifts must come from the nanostructure. In the far-field Raman spectra, the peak shift caused by the ridge is very small because the spatial resolution of far-field Raman is larger than the nanoridge, and thus the signal from the ridge is obscured by the signal from the large neighboring flat area. Our Raman microscope has a spatial resolution of 1 µm, while the spatial resolution of TERS is in the same magnitude with the tip radius.[36,37] (The tip used in this experiment had a tip radius of 75 nm.)

Generally, the shift of the G' band to a lower wavenumber is associated with a phonon softening process induced by bond lengthening from tensile (stretching) strain.[25,55] Nevertheless, if we compare the G' band positions of our study to the 2674 cm^{-1} of free-standing graphene with no external strain (Beriaud et al., measured with the same excitation wavelength as in our experiment),[56] the G' band on the ridge (2691 cm^{-1}) is closer to free-standing graphene than the G' band of nearby flat areas (2700 cm^{-1}). Therefore, the band downshift observed on this nanostructure is the result of reduced compressive strain relative to the nearby area, rather than tensile strain. The strain presents on the ridge and flat area can be calculated by the relationship:[24]

$$\omega_{G'} = \omega^{0}_{G'} + \Delta\omega^{m}_{G'} + \Delta\omega^{e}_{G'} \tag{1}$$

where $\omega_{G'}$, $\omega^{0}_{G'}$, $\Delta\omega^{m}_{G'}$, and $\Delta\omega^{e}_{G'}$ are the observed G' band position, unstrained and undoped G' band position, position shift cause by mechanical stain, and shift cause by carrier doping, respectively. The mechanical part then can be calculated by:[23]

$$\Delta\omega^{m}_{G'} = -\omega^{0}_{G'}\gamma^{uniaxial}_{G'}(1-\nu)\varepsilon \tag{2}$$

for uniaxial strain, where $\gamma_{G'}^{uniaxial}$ is the Grüneisen parameter for the G' band, ν is Poisson's ratio for graphene or substrate and ε is the strain of the graphene sheet. For biaxial strain, which assumes equivalent strain on both axes, the equation is:

$$\Delta\omega_{G'}^{m} = -2\omega_{G'}^{0}\gamma_{G'}^{biaxial}\varepsilon \tag{3}$$

Although the carrier doping term is difficult to evaluate, by assuming negligible doping difference between graphene on the ridge and the surrounding area, the doping term can be eliminated in the calculation of the strain difference between two measurement points.

Relative strain on each point across the ridge in Figure 3d and 3e is calculated using $\omega_{G'}^{0} = 2674\ cm^{-1}$ from unstrained suspended graphene[56], a Grüneisen parameter $\gamma_{G'}^{uniaxial} = 2.7$ for uniaxial strain[23,25], $\gamma_{G'}^{biaxial} = 2.8$ for biaxial strain[24], Poisson's ratio $\nu = 0.231$ for SiC[57] due to the attraction of graphene to the substrate[25], and the TERS spectra on point 1 (flat area) as a reference. It is worth noting that many references report differing Grüneisen parameter values for G' band and Poisson's ratio values for graphene/SiC.[23–25,55,57–59] The details of the calculation, including calculated strain using different constant values, are available in the supporting information.

With the results from the TERS spectra, the maximum strain difference is found on point 5 (ridge) with uniaxial strain of $(1.6 \pm 0.2) \times 10^{-3}$ and biaxial strain of $(5.8 \pm 0.6) \times 10^{-4}$. The positive values denote smaller compressive strain on the ridge (since compressive strain is assigned with negative value, a positive difference implies reduced compressive strain). This is an evidence for the proposed mechanism of Prakash et al.[12] and Sun et al.[11] that nanoridges of SiC-grown graphene form as a relief from the strain in epitaxial graphene grown on SiC. This is also the first time that strain on a nanoridge of epitaxial graphene was measured using TERS. Our calculated strain value for each point falls between the empirical minimum of 1×10^{-3} and the theoretical maximum of 8×10^{-3} reported by Ferralis et al.[26]

while Prakash et al. reported an unusually high value of 4.4×10^{-2} calculated from AFM topology.[12]

If the peak positions from far-field Raman spectra are used, the calculated uniaxial and biaxial strain on the ridge are only $(2.7 \pm 1.7) \times 10^{-4}$ and $(1.0 \pm 0.6) \times 10^{-4}$ relative to flat area (Figure 3d and 3e), respectively. The lesser values compared to the TERS results can be attributed to the size of the ridge structure being smaller than the spatial resolution of normal Raman spectroscopy. This clearly demonstrates the limitations of far-field Raman spectroscopy on the characterization of graphene nanostructures.

Regarding the strain direction, Schmidt et al. suggested that uniaxial strain would cause the G peak to split into two components. Therefore the strain should be biaxial when there is no splitting.[24] However, any splitting (if exist) from small strain, such as in our case, is too small to be resolved.[23] By positing that nanoridges are a result of strain relief in the direction across the width of the ridge, the actual strain in our sample should be between purely uniaxial and biaxial strain.

Figure 3c, 3d and 3e can be discussed from another aspect. For each measurement point, band position and strain from TERS spectrum can be compared with the values from far-field spectrum to show the difference between graphene in the area near and far from the nanostructure. In overall, G' band positions are lower in TERS compared to far-field spectra, with the difference from around 3 cm^{-1} in the flat areas to as high as 11.1 cm^{-1} on the ridge. This indicate that the compressive strain of graphene is strongest in the outer region (which probed by far-field Raman spectroscopy but not TERS), a little weaker in the area around the ridge, and weakest on the ridge.

TERS spectra of crack sub-microstructure

Figure 4a represents an AFM image of a crack structure. From the AFM topology line profile in Figure 4a, one can see that this crack is roughly 200 nm wide and 20 nm deep. The measured depth is a minimal value since the TERS tip used in this experiment has a 75 nm tip radius. The actual depth might be much greater if the deeper part of the crack is narrower than 75 nm. Since graphene cannot be thicker than a few nanometers, this crack undoubtedly extends into the SiC substrate. Five TERS and far-field Raman spectra were acquired across the crack as shown in Figure 4b. A G' peak for each point is shown in Figure 4b and 4c. The FWHM of the G' peak from every point is less than 25 cm^{-1} for both subtracted (TERS) and tip retracted (far-field Raman) spectra, corresponding to single layer graphene.

Figure 4b clearly demonstrates a diminished intensity of G' peak in the TERS spectra from the middle of the crack. However, the peak intensity in the TERS measurements also depends on tip-laser coupling precision and can be varied, even for the measurements on the same point. Thus, we use the SiC transverse optical phonon peak (SiC E_2 at 776 cm^{-1}) as an internal standard. The plot of the peak height ratio between graphene G' and SiC E_2 from the TERS spectra (Figure 4c) matches well with the AFM line profile. Peak height ratio is significantly reduced in the center of the crack, indicating lesser or absent graphene content. For points just outside the crack (points 2 and 4), while the G' peak height is lower (Figure 4b), the G' and SiC E_2 height ratio in Figure 4c is similar to points that far from the crack, emphasizing the importance of normalization using the SiC E_2 peak. This reduced $I_{G'}/I_{SiC}$ ratios in the spectrum from the crack center cannot be detected by far-field Raman spectroscopy, as shown in Figure 4c.

Conclusion

TERS and far-field Raman spectra from step, ridge, and crack structures of epitaxial graphene were studied. The step nanostructure, which originates from the underlying SiC and contains single-layer graphene on both step sides, does not significantly affect the TERS and far-field Raman spectra. In the TERS spectra, the ridge structure produced 8.7 cm^{-1} lower wavenumber of G' band, suggesting a relaxation of compressive strain with respect to the surrounding area. Using the strain-G' peak position equation, the strain difference between a ridge and its surrounding area is 1.6×10^{-3} and 6.0×10^{-4} for uniaxial and biaxial strain, respectively. In the far-field Raman spectra, the peak shift is much smaller due to inadequate spatial resolution. The TERS spectra of a crack structure show a reduced graphene/SiC signal ratio, which cannot be probed by far-field Raman spectroscopy. These results suggest that TERS is a powerful technique in the characterization of nano/sub-micro structures on epitaxial graphene.

References

(1) Castro Neto, A. H.; Guinea, F.; Peres, N. M. R.; Novoselov, K. S.; Geim, A. K. The Electronic Properties of Graphene. *Rev. Mod. Phys.* **2009**, *81*, 109–162.

(2) Allen, M. J.; Tung, V. C.; Kaner, R. B. Honeycomb Carbon: A Review of Graphene. *Chem. Rev.* **2010**, *110*, 132–145.

(3) Shao, Y.; Wang, J.; Wu, H.; Liu, J.; Aksay, I. A.; Lin, Y. Graphene Based Electrochemical Sensors and Biosensors: A Review. *Electroanalysis* **2010**, *22*, 1027–1036.

(4) Novoselov, K. S.; Geim, A. K.; Morozov, S. V.; Jiang, D.; Zhang, Y.; Dubonos, S. V.; Grigorieva, I. V.; Firsov, A. A. Electric Field Effect in Atomically Thin Carbon Films. *Science* **2004**, *306*, 666–669.

(5) Ushio, S.; Yoshii, A.; Tamai, N.; Ohtani, N.; Kaneko, T. Epitaxial Graphene Growth on 4H-SiC (0001) with Precisely Controlled Step- Terrace Surface by High Temperature Annealing Above 2000 °C in UHV. *Phys. Status Solidi C* **2011**, *8*, 580–582.

(6) Emtsev, K. V.; Bostwick, A.; Horn, K.; Jobst, J.; Kellogg, G. L.; Ley, L.; McChesney, J. L.; Ohta, T.; Reshanov, S. A.; Röhrl, J.; et al. Towards Wafer-size Graphene Layers by Atmospheric Pressure Graphitization of Silicon Carbide. *Nat. Mater.* **2009**, *8*, 203–207.

(7) Velez-Fort, E.; Mathieu, C.; Pallecchi, E.; Pigneur, M.; Silly, M. G.; Belkhou, R.; Marangolo, M.; Shukla, A.; Sirotti, F.; Ouerghi, A. Epitaxial Graphene on 4H-SiC(0001) Grown Under Nitrogen Flux: Evidence of Low Nitrogen Doping and High Charge Transfer. *ACS Nano* **2012**, *6*, 10893–10900.

(8) Hass, J.; Varchon, F.; Millán-Otoya, J. E.; Sprinkle, M.; Sharma, N.; de Heer, W. A.; Berger, C.; First, P. N.; Magaud, L.; Conrad, E. H. Why Multilayer Graphene on 4H-SiC(0001¯) Behaves Like a Single Sheet of Graphene. *Phys. Rev. Lett.* **2008**, *100*, 125504.

(9) Luxmi; Fisher, P. J.; Srivastava, N.; Feenstra, R. M.; Sun, Y.; Kedzierski, J.; Healey, P.; Gu, G. Morphology of Graphene on SiC(0001¯) Surfaces. *Appl. Phys. Lett.* **2009**, *95*, 073101.

(10) Low, T.; Guinea, F.; Katsnelson, M. I. Gaps Tunable by Electrostatic Gates in Strained Graphene. *Phys. Rev. B* **2011**, *83*, 195436.

(11) Sun, G. F.; Jia, J. F.; Xue, Q. K.; Li, L. Atomic-scale Imaging and Manipulation of Ridges on Epitaxial Graphene on 6H-SiC(0001). *Nanotechnology* **2009**, *20*, 355701.

(12) Prakash, G.; Capano, M. A.; Bolen, M. L.; Zemlyanov, D.; Reifenberger, R. G. AFM Study of Ridges in Few-layer Epitaxial Graphene Grown on the Carbon-face of 4H–SiC. *Carbon* **2010**, *48*, 2383–2393.

(13) Wang, F.; Liu, G.; Rothwell, S.; Nevius, M.; Tejeda, A.; Taleb-Ibrahimi, A.; Feldman, L. C.; Cohen, P. I.; Conrad, E. H. Wide-Gap Semiconducting Graphene from Nitrogen-Seeded SiC. *Nano Lett.* **2013**, *13*, 4827–4832.

(14) Biedermann, L. B.; Bolen, M. L.; Capano, M. A.; Zemlyanov, D.; Reifenberger, R. G. Insights into Few-layer Epitaxial Graphene Growth on 4H-SiC(0001¯) Substrates from STM Studies. *Phys. Rev. B* **2009**, *79*, 125411.

(15) Xu, P.; Barber, S. D.; Schoelz, J. K.; Ackerman, M. L.; Qi, D.; Thibado, P. M.; Wheeler, V. D.; Nyakiti, L. O.; Myers-Ward, R. L.; Jr, C. R. E.; et al. Atomic-scale Movement Induced in Nanoridges by Scanning Tunneling Microscopy on Epitaxial Graphene Grown on 4H-SiC(0001). *J. Vac. Sci. Technol. B* **2013**, *31*, 04D101.

(16) Hicks, J.; Tejeda, A.; Taleb-ibrahimi, A.; Nevius, M. S.; Wang, F.; Shepperd, K.; Palmer, J.; Bertran, F.; Le Fèvre, P.; Kunc, J.; et al. A Wide-bandgap Metal-semiconductor-metal Nanostructure Made Entirely from Graphene. *Nat. Phys.* **2013**, *9*, 49–54.

(17) Stadler, J.; Schmid, T.; Zenobi, R. Nanoscale Chemical Imaging of Single-Layer Graphene. *ACS Nano* **2011**, *5*, 8442–8448.

(18) Cançado, L. G.; Jorio, A.; Ferreira, E. H. M.; Stavale, F.; Achete, C. A.; Capaz, R. B.; Moutinho, M. V. O.; Lombardo, A.; Kulmala, T. S.; Ferrari, A. C. Quantifying Defects in Graphene via Raman Spectroscopy at Different Excitation Energies. *Nano Lett.* **2011**, *11*, 3190–3196.

(19) Eckmann, A.; Felten, A.; Verzhbitskiy, I.; Davey, R.; Casiraghi, C. Raman Study on Defective Graphene: Effect of the Excitation Energy, Type, and Amount of Defects. *Phys. Rev. B* **2013**, *88*, 035426.

(20) Bracamonte, M. V.; Lacconi, G. I.; Urreta, S. E.; Foa Torres, L. E. F. On the Nature of Defects in Liquid-Phase Exfoliated Graphene. *J. Phys. Chem. C* **2014**, *118*, 15455–15459.

(21) Krauss, B.; Nemes-Incze, P.; Skakalova, V.; Biro, L. P.; Klitzing, K. von; Smet, J. H. Raman Scattering at Pure Graphene Zigzag Edges. *Nano Lett.* **2010**, *10*, 4544–4548.

(22) Strudwick, A. J.; Creeth, G. L.; Johansson, N. a. B.; Marrows, C. H. Probing Residual Strain in Epitaxial Graphene Layers on 4H-SiC(0001¯) with Raman Spectroscopy. *Appl. Phys. Lett.* **2011**, *98*, 051910.

(23) Mohiuddin, T. M. G.; Lombardo, A.; Nair, R. R.; Bonetti, A.; Savini, G.; Jalil, R.; Bonini, N.; Basko, D. M.; Galiotis, C.; Marzari, N.; et al. Uniaxial Strain in Graphene by Raman Spectroscopy: G Peak Splitting, Grüneisen Parameters, and Sample Orientation. *Phys. Rev. B* **2009**, *79*, 205433.

(24) Schmidt, D. A.; Ohta, T.; Beechem, T. E. Strain and Charge Carrier Coupling in Epitaxial Graphene. *Phys. Rev. B* **2011**, *84*, 235422.

(25) Ferralis, N. Probing Mechanical Properties of Graphene with Raman Spectroscopy. *J. Mater. Sci.* **2010**, *45*, 5135–5149.

(26) Ferralis, N.; Maboudian, R.; Carraro, C. Evidence of Structural Strain in Epitaxial Graphene Layers on 6H-SiC(0001). *Phys. Rev. Lett.* **2008**, *101*, 156801.

(27) Malard, L. M.; Pimenta, M. A.; Dresselhaus, G.; Dresselhaus, M. S. Raman Spectroscopy in Graphene. *Phys. Reports* **2009**, *473*, 51–87.

(28) Rao, R.; Podila, R.; Tsuchikawa, R.; Katoch, J.; Tishler, D.; Rao, A. M.; Ishigami, M. Effects of Layer Stacking on the Combination Raman Modes in Graphene. *ACS Nano* **2011**, *5*, 1594–1599.

(29) Graf, D.; Molitor, F.; Ensslin, K.; Stampfer, C.; Jungen, A.; Hierold, C.; Wirtz, L. Spatially Resolved Raman Spectroscopy of Single- and Few-Layer Graphene. *Nano Lett.* **2007**, *7*, 238–242.

(30) Saito, Y.; Verma, P.; Masui, K.; Inouye, Y.; Kawata, S. Nano-scale Analysis of Graphene Layers by Tip-enhanced Near-field Raman Spectroscopy. *J. Raman Spectrosc.* **2009**, *40*, 1434–1440.

(31) Hoffmann, G. G.; Xue, L.; Loos, J.; de With, G. High-Resolution Tip-Enhanced Raman Mapping. *Macromol. Symp.* **2011**, *305*, 26–42.

(32) Ghislandi, M.; Hoffmann, G. G.; Tkalya, E.; Xue, L.; With, G. D. Tip-Enhanced Raman Spectroscopy and Mapping of Graphene Sheets. *Appl. Spectrosc. Rev.* **2012**, *47*, 371–381.

(33) Choi, M.; Son, J.; Choi, H.; Shin, H.-J.; Lee, S.; Kim, S.; Lee, S.; Kim, S.; Lee, K.-R.; Kim, S. J.; et al. In-situ Raman Spectroscopy of Current-carrying Graphene Microbridge. *J. Raman Spectrosc.* **2014**, *45*, 168–172.

(34) Tedesco, J. L.; Jernigan, G. G.; Culbertson, J. C.; Hite, J. K.; Yang, Y.; Daniels, K. M.; Myers-Ward, R. L.; Jr, C. R. E.; Robinson, J. A.; Trumbull, K. A.; et al. Morphology Characterization of Argon-mediated Epitaxial Graphene on C-face SiC. *Appl. Phys. Lett.* **2010**, *96*, 222103.

(35) Vizzini, S.; Enriquez, H.; Chiang, S.; Oughaddou, H.; Soukiassian, P. Nano-structures Developing at the Graphene/silicon Carbide Interface. *Surf. Sci.* **2011**, *605*, L6–L11.

(36) Verma, P.; Ichimura, T.; Yano, T.; Saito, Y.; Kawata, S. Nano-imaging through Tip-enhanced Raman Spectroscopy: Stepping Beyond the Classical Limits. *Laser Photonics Rev.* **2009**, *4*, 548–561.

(37) Domke, K. F.; Pettinger, B. Studying Surface Chemistry Beyond the Diffraction Limit: 10 Years of TERS. *ChemPhysChem* **2010**, *11*, 1365–1373.

(38) Deckert, V. Tip-Enhanced Raman Spectroscopy. *J. Raman Spectrosc.* **2009**, *40*, 1336–1337.

(39) Hayazawa, N.; Inouye, Y.; Sekkat, Z.; Kawata, S. Metallized Tip Amplification of Near-field Raman Scattering. *Opt. Commun.* **2000**, *183*, 333–336.

(28) Yano, T.; Kawata, S. Tip-Enhanced Raman Spectroscopy (TERS) for Nanoscale Imaging and Analysis. In *Frontiers of surface-enhanced raman scattering: single-nanoparticles and single cells*; Ozaki, Y., Kneipp, K., Aroca, R., Eds.; John Wiley & Sons, Inc: Chichester, West Sussex, 2014; pp 142-161.

(41) Kawata, S.; Inouye, Y.; Verma, P. Plasmonics for Near-field Nano-imaging and Superlensing. *Nat. Photonics* **2009**, *3*, 388–394.

(42) Domke, K. F.; Pettinger, B. Tip-enhanced Raman Spectroscopy of 6H-SiC with Graphene Adlayers: Selective Suppression of E1 Modes. *J. Raman Spectrosc.* **2009**, *40*, 1427–1433.

(43) Ren, B.; Picardi, G.; Pettinger, B. Preparation of Gold Tips Suitable for Tip-enhanced Raman

Spectroscopy and Light Emission by Electrochemical Etching. *Rev. Sci. Instrum.* **2004**, *75*, 837–841.

(44) Hoffmann, G. G.; de With, G.; Loos, J. Micro-Raman and Tip-Enhanced Raman Spectroscopy of Carbon Allotropes. *Macromol. Symp.* **2008**, *265*, 1–11.

(45) Wang, P.; Zhang, D.; Li, L.; Li, Z.; Zhang, L.; Fang, Y. Reversible Defect in Graphene Investigated by Tip-Enhanced Raman Spectroscopy. *Plasmonics* **2012**, *7*, 555–561.

(46) Rickman, R. H.; Dunstan, P. R. Enhancement of Lattice Defect Signatures in Graphene and Ultrathin Graphite Using Tip-enhanced Raman Spectroscopy: Enhancement of Defect Signatures in Graphene Using Tip-enhanced Raman. *J. Raman Spectrosc.* **2014**, *45*, 15–21.

(47) Poliani, E.; Nippert, F.; Maultzsch, J. Effect of Gap Modes on Graphene and Multilayer Graphene in Tip-enhanced Raman Spectroscopy. *Phys. Status Solidi B* **2012**, *249*, 2511–2514.

(48) Suzuki, T.; Itoh, T.; Vantasin, S.; Minami, S.; Kutsuma, Y.; Ashida, K.; Kaneko, T.; Morisawa, Y.; Miura, T.; Ozaki, Y. Tip-enhanced Raman Spectroscopic Measurement of Stress Change in the Local Domain of Epitaxial Graphene on the Carbon Face of 4H-SiC(0001¯). *Phys. Chem. Chem. Phys.* **2014**, *16*, 20236–20240.

(49) Sorieul, S.; Costantini, J.-M.; Gosmain, L.; Thomé, L.; Grob, J.-J. Raman Spectroscopy Study of Heavy-ion-irradiated α-SiC. *J. Phys. Condens. Matter* **2006**, *18*, 5235.

(50) Rao, R.; Tishler, D.; Katoch, J.; Ishigami, M. Multiphonon Raman Scattering in Graphene. *Phys. Rev. B* **2011**, *84*, 113406.

(51) Lee, D. S.; Riedl, C.; Krauss, B.; von Klitzing, K.; Starke, U.; Smet, J. H. Raman Spectra of Epitaxial Graphene on SiC and of Epitaxial Graphene Transferred to SiO2. *Nano Lett.* **2008**, *8*, 4320–4325.

(52) Yue, Y.; Zhang, J.; Wang, X. Micro/Nanoscale Spatial Resolution Temperature Probing for the Interfacial Thermal Characterization of Epitaxial Graphene on 4H-SiC. *Small* **2011**, *7*, 3324–3333.

(53) Mounet, N.; Marzari, N. First-principles Determination of the Structural, Vibrational and Thermodynamic Properties of Diamond, Graphite, and Derivatives. *Phys. Rev. B* **2005**, *71*, 205214.

(54) Frank, O.; Tsoukleri, G.; Parthenios, J.; Papagelis, K.; Riaz, I.; Jalil, R.; Novoselov, K. S.; Galiotis, C. Compression Behavior of Single-Layer Graphenes. *ACS Nano* **2010**, *4*, 3131–3138.

(55) Ni, Z. H.; Yu, T.; Lu, Y. H.; Wang, Y. Y.; Feng, Y. P.; Shen, Z. X. Uniaxial Strain on Graphene: Raman Spectroscopy Study and Band-Gap Opening. *ACS Nano* **2008**, *2*, 2301–2305.

(56) Berciaud, S.; Ryu, S.; Brus, L. E.; Heinz, T. F. Probing the Intrinsic Properties of Exfoliated Graphene: Raman Spectroscopy of Free-Standing Monolayers. *Nano Lett.* **2009**, *9*, 346–352.

(57) Luo, X.; Goel, S.; Reuben, R. L. A Quantitative Assessment of Nanometric Machinability of Major Polytypes of Single Crystal Silicon Carbide. *J. Eur. Ceram. Soc.* **2012**, *32*, 3423–3434.

(58) Metzger, C.; Rémi, S.; Liu, M.; Kusminskiy, S. V.; Castro Neto, A. H.; Swan, A. K.; Goldberg, B. B. Biaxial Strain in Graphene Adhered to Shallow Depressions. *Nano Lett.* **2010**, *10*, 6–10.

(59) Karmann, S.; Helbig, R.; Stein, R. A. Piezoelectric Properties and Elastic Constants of 4H and 6H SiC at Temperatures 4–320 K. *J. Appl. Phys.* **1989**, *66*, 3922.

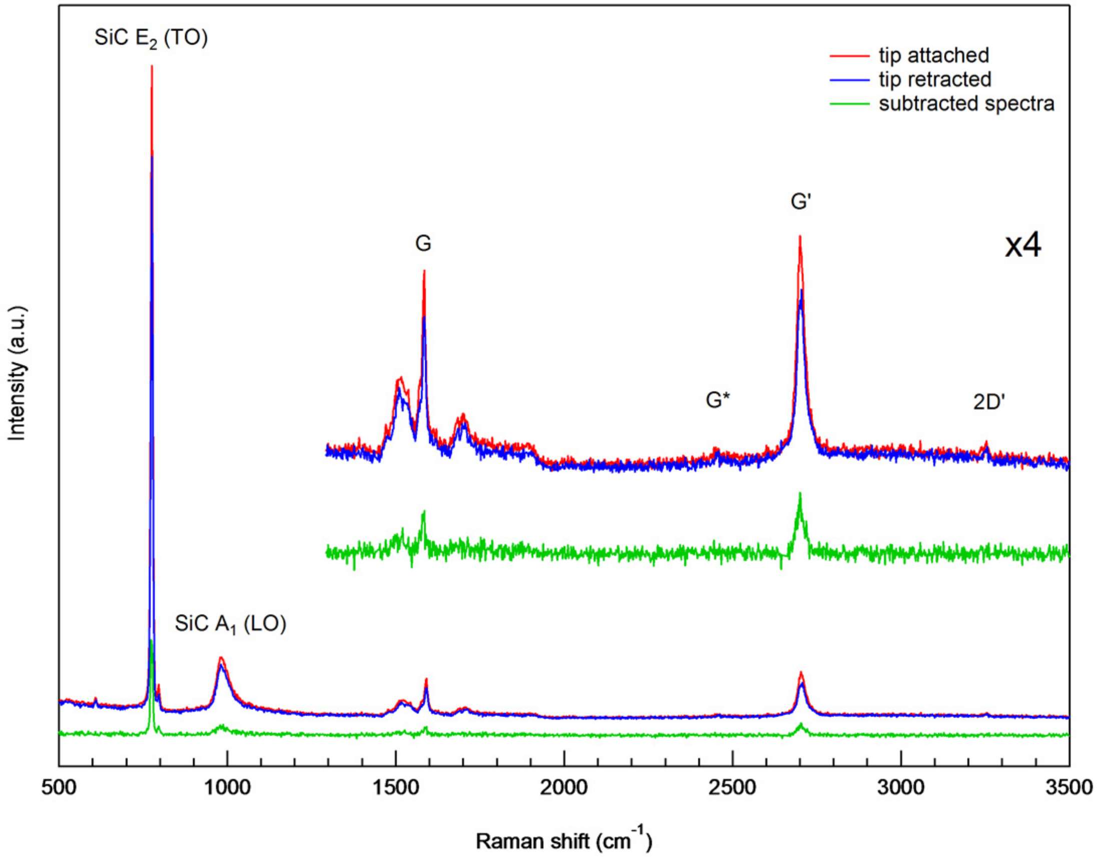

Figure 1 Tip-attached, tip-retracted, and subtracted Raman spectra of C-face epitaxial graphene from area with single layer graphene.

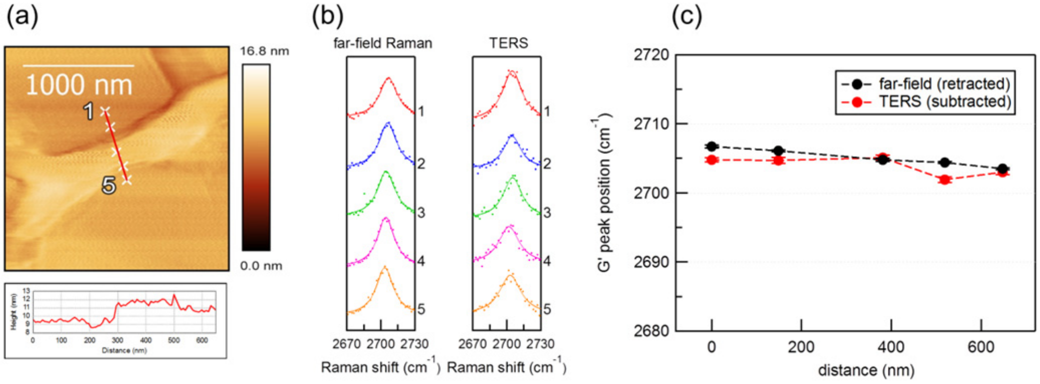

Figure 2 TERS measurement on step structure. (a) AFM topology image and line height profile. (b) G' band in far-field Raman and TERS spectra from five measurement points shown in (a). (c) Peak position of each G' band in (b), plotted against distances from point 1 along the line profile in (a). Error bars in (c) were calculated from uncertainties in Lorentzian fitting. Some errors bars are too small to be clearly visible.

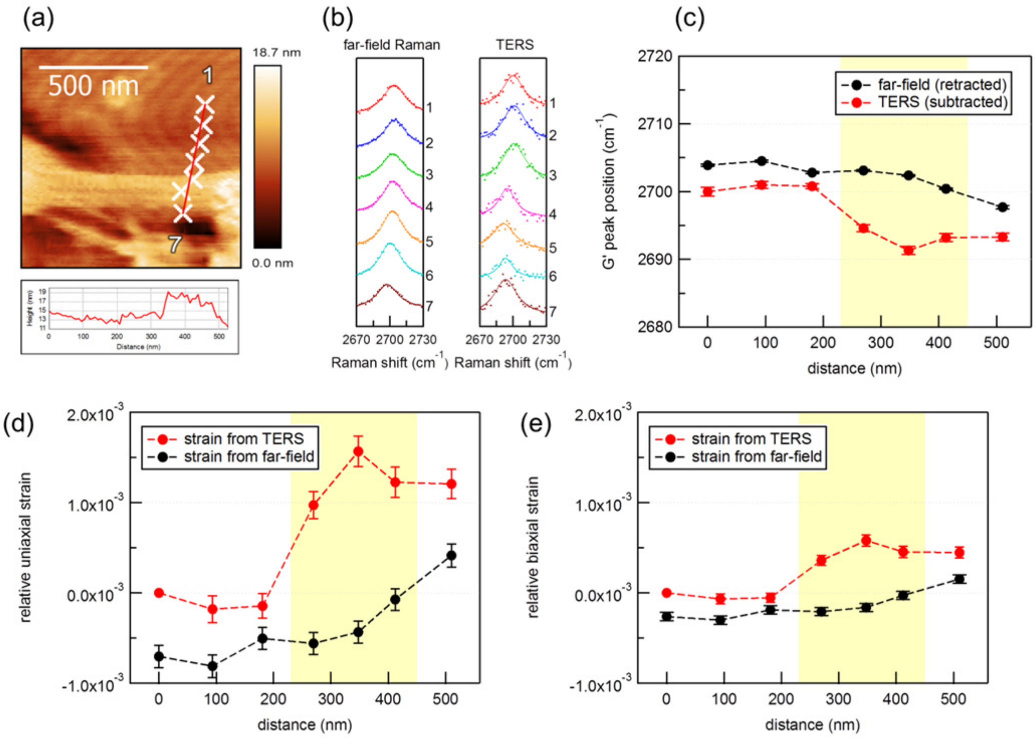

Figure 3 TERS measurement on ridge structure. (a) AFM topology image and line height profile. (b) G' band in far-field Raman and TERS spectra from seven measurement points shown in (a). (c) Peak position of each G' band in (b), plotted against distances from point 1 along the line profile in (a). (d),(e) Calculated relative uniaxial and biaxial strain on each point, plot in the same fashion as (c), respectively. Error bars in (c), (d), and (e) were calculated from uncertainties in Lorentzian fitting and Grüneisen parameter.

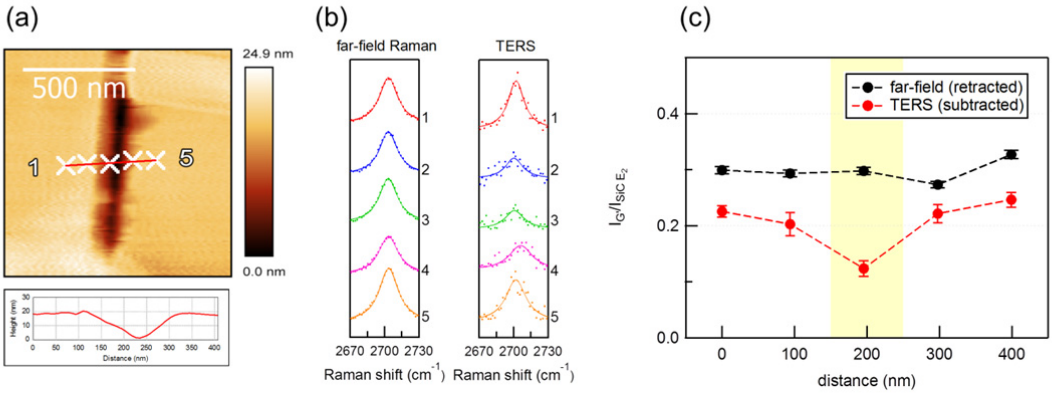

Figure 4 TERS measurement on crack structure. (a) AFM topology image and line height profile. (b) G' band in far-field Raman and TERS spectra from five measurement points shown in (a). (c) $I_{G'}/I_{SiC\ E2}$ intensity ratio of each spectra in (b), plotted against distances from point 1 along the line profile in (a). Error bars in (c) were calculated from uncertainties in Lorentzian fitting.

Chapter II: Characterization of SiC-grown epitaxial graphene microisland using tip-enhanced Raman spectroscopy

Abstract

Single-layer graphene microislands with smooth edges and no visible grain boundary were epitaxially grown on the C-face of 4H-SiC and then characterized in the nanoscale using tip-enhanced Raman spectroscopy (TERS). Although these graphene islands appear highly homogeneous in micro Raman imaging, TERS reveals the nanoscale strain variation caused by ridge nanostructures. A G′ band position shift up to 9 cm^{-1} and a band broadening up to 30 cm^{-1} are found in TERS spectra obtained from nanoridges, which is explained by compressive strain relaxation mechanism. The small size and refined nature of the graphene islands helps in minimizing the inhomogeneity caused by macroscale factors, and allows a comparative discussion between proposed mechanisms of nanoridges formation.

Introduction

Epitaxial graphene grown on SiC is considered to be useful in a wide range of applications due to its large sheet area, low defects, transparent substrate, and circuit-ready capability without the need of substrate transfer.[1–4] One of its interesting properties is nanostructures such as nanoridges, nanocracks, and nanosteps, which are created during the graphene synthesis.[5–9] These features are more evident in graphene grown on the C-face of SiC than on the Si-face due to the weaker graphene-substrate attraction in the former case.[10,11] The presence of nanostructures causes a deformation of graphene, from a perfectly two-dimensional flat object into a sheet with curvatures. It is known that curvatures alter graphene both physically and electronically.[12] Thus, the manipulations of the nanostructures could conceivably be used to create interesting graphene samples, such as graphene with adjustable band gap.[8] Since these effects from nanostructures should not be neglected, techniques with a nanoscale spatial resolution are crucial for graphene characterization. Scanning tunnelling microscopy and atomic force microscopy (STM/AFM),[5,6] scanning tunnelling spectroscopy (STS),[13] angle-resolved photoemission spectroscopy (ARPES),[14] and high-angle annulardark-field scanning tunnelling electron microscopy (HAADF STEM)[15] have been used to investigate the nanoscale structures of epitaxial graphene grown on SiC, along with their effects on electronic properties.

Raman spectroscopy has the capability to determine a great deal of information about graphene such as the number of layers,[16–20] doping,[21–23] strain,[22,24,25] defects,[23,26] etc. However, due to the diffraction limit of light, its spatial resolution is insufficient to study each nanofeature individually. Tip-enhanced Raman spectroscopy (TERS) is a technique that exploits information-richness of Raman spectroscopy and nanoscale resolving power of STM/AFM. By using a metallic nanotip, plasmon enhancement is confined to the small area at the tip apex and the Raman signal solely from this area can be detected.[27–31] Due to its excellent spatial resolution, TERS has been used in graphene studies, especially in the investigation of small features such as edge boundaries,[18–20,32,33] nanodefects,[34–36] gap modes,[37,38] and local strain.[9,39,40] Using this technique, our previous study presented Raman spectra of ridge, crack, and step nanostructures on epitaxial graphene, which revealed direct evidence for the proposed mechanism that the nanoridges are formed through a relaxation against compressive strain.[9] However, an alternative possible mechanism, in which Si vapour is trapped between graphene and SiC substrate and then accumulates into ridges, has also been suggested.[41] It is known that under high temperature, additional deposited silicon can diffuse through graphene and intercalate it from the SiC substrate, this process occurs on both C face and Si face of SiC.[42–44] On the Si-face, it has been shown that nanostructures can be created by the process.[44]

The difficulties in the mechanism analysis arise from the complexity of the samples. Some previous studies on nanoridges were done using few layers graphene, and the authors suggested that layer effects must be put in the consideration.[5,7] Large sheet graphene might acquire inherent doping and strain inhomogeneity, both of which are highly dependent on the growth pattern.[22] Grain boundaries and defects can also be a hindrance. To eliminate these interfering factors, this study employs epitaxial graphene microislands on the C-face of SiC as an ideal sample for nanostructures investigation. These graphene microislands have no visible grain boundary, and also contain no irregular edges like those found in the large-sheet epitaxial graphene of our previous study. They are unaffected by macro-scale anisotropic interaction caused by imperfection of SiC. During the synthesis, the inhomogeneity of temperature throughout the graphene sheet should be minimal, as the islands are just several micrometres in size. The single-layer nature and growth pattern of the graphene islands are also obvious. In this study, one of the highly regular graphene islands was investigated with TERS, revealing the effects that solely come from graphene nanoridges. This is also the first time that TERS results from multiple graphene nanoridges are compared and discussed.

In addition, studying the properties of graphene microislands is also very interesting in itself. Graphene islands are known to have unique properties such as temperature effects,[45] a shape and size dependent on Ar pressure in the synthesis chamber,[46] and size dependent plasmon.[47] The interest in understanding the in-depth properties of graphene islands and their growth mechanism is therefore extensive,[46,48] and so the understanding of their nanostructures is inevitably needed. We believe that the nano-characterization presented in this study would yield further insights on the properties of graphene islands that originate in nanoscale.

Experimental Section

Synthesis of graphene microislands

On-axis 4H-SiC $(000\bar{1})$ wafer was engraved by YVO_4 laser to create pits with a size of several hundred micrometres. Si vapour etching was then used to make the pits bottom became step-free, large $(000\bar{1})$ basal planes. After properly washed, the wafer was heated for 15 minutes in a semi-closed TaC container at 1800 °C and controlled argon atmosphere with 6.67 kPa pressure. The epitaxial graphene microislands then grew on the defects in the basal planes of SiC. Since the defects are rare, it was easy to find basal planes with only single defect. Thus the graphene islands shown in this study were the only single island in their pits and thus not interfered by other island or other defect.

This technique has an advantage that the amount of graphene growth can be precisely controlled by the adjustment of temperature and Si partial pressure. The details of the synthesis were elaborately discussed in our previous paper.[3]

2.2 Characterization of a graphene microisland

AFM topography images of a graphene island were collected using a silicon cantilever with 20 nm tip radius (UNISOKU Co. LTD). The tip was controlled by non-contact mode to prevent any deformation on the graphene nanostructures. Since moisture can affect non-contact AFM, the nitrogen flow was used to ensure < 1.0 % humidity during the scanning.

Raman spectra were measured by a Raman spectrometer equipped with a liquid nitrogen-cooled CCD detector (Photon Design Nanostar NFRSM800). The excitation laser was a DPSS laser with 514 nm wavelength (Cobolt Fandago 25). The magnification and numerical aperture (NA) of the objective lens were X90 and 0.71, respectively. The confocal setup allows the spatial resolution of about 500 nm.

Etched bulk silver tips with ~50 nm apex radius (UNISOKU Co. LTD) were used for TERS measurements. They were controlled by the same fashion as the AFM tips mentioned above. The TERS tips lie 45° from the sample plane. The micro Raman system described in the above paragraph was used to collect TERS signal. Thus, the TERS setup in this study was top-illumination and top-collection. Each acquisition was done with laser power of 0.10 mW and exposure time of 720 seconds.

Since the laser spot of micro-Raman system was larger than TERS tips, each signal in the TERS measurement is composed of tip-enhanced component (near-field) and unenhanced out-of-tip component (far-field). For every measurement point, a spectrum was collected in tip-attached position to get both near-field and far-field signal. Then, another spectrum was collected in tip-retracted position to acquire only the far-field component. The subtraction of the former spectrum by the latter one yields solely near-field component, and is presented as 'TERS spectrum' in this paper.

Results and discussion

Although the graphene microisland appears highly homogeneous in the micro Raman imaging, the exceeding spatial resolution of TERS reveals a different picture at the nanoscale level. The relationship between graphene topology and TERS spectra is shown in Figure 3, in which the TERS spectra from a nanoridge and flat area are compared. G′ band is chosen in this analysis because G band is interfered by SiC bands around 1600 cm^{-1}. Both bands shift to the same direction in response of strain, thus using only G′ band should suffice. G′ position shift is also more sensitive to strain than G band. The nanoridge (ridge #1) in Figure 3b was ~2.0 nm in eight and ~70 nm in width, whereas the target flat area (flat #5) had a height variation of less than 0.5 nm.

In Figure 3d, it is clear that the G′ bands in the TERS spectra of the ridge and flat area have significantly different Raman shifts (2682 cm^{-1} vs 2691 cm^{-1}) but the difference is not pronounced in the far-field Raman spectra in Figure 3e (2691 cm^{-1} vs 2692 cm^{-1}). This difference between the ridge and flat area is clearly demonstrated in Figure 4. The figure presents TERS and far-field Raman spectra from eight points from nanoridges (Figure 4a) and flat areas (Figure 4b). Noted that on the nanoridges, the standard deviations of the G′ band position and FWHM are significantly larger for the TERS spectra than those of the far-field spectra. Moreover, the band positions in TERS spectra from nanoridges shows significant downshifts, whereas the band positions in the TERS spectra from the flat areas remain almost equal to the far-field spectra. It is safe to say that in the far-field Raman spectra, the signal from the ridge is overwhelmed by the signal from the much larger surrounding flat area. This is a crucial point for graphene island samples, as it means that graphene islands which appear to have a homogeneous strain might actually exhibit a variation in the nanoscale. As discussed and shown above, other potential sources of irregularity (e.g., inherent strain variation in macro scale, grain boundary effects, and layer effects) are minimal or non-existent for this graphene sample. Therefore, it can be concluded that the nanoscale inhomogeneity must come from the nanoridges.

From the G′ band position in Figure 3, the strain difference between the ridge and flat area can be calculated using the following equation:[9,54]

$$\Delta\varepsilon = -\frac{\omega_{G'}^{ridge} - \omega_{G'}^{flat}}{\omega_{G'}^{0}\gamma_{G'}^{uniaxial}(1-\nu)} \tag{1}$$

where $\omega_{G'}^{ridge}$, $\omega_{G'}^{flat}$, and $\omega_{G'}^{0}$ represent the G′ band position from the ridge, the flat area, and unstrained graphene (2674 cm^{-1} with 514 nm excitation wavelength), respectively.[61] $\gamma_{G'}^{uniaxial}$ is the uniaxial Grüneisen parameter for the G′ band of graphene (2.7),[24,54] and ν is the Poisson's ratio of SiC (0.231).[62] The Poisson's ratio of SiC was chosen here instead of that of graphene because SiC-grown epitaxial graphene attaches strongly to the substrate.[24] Note that this equation is based on a uniaxial strain model that assumes a strain in only one direction, which is not perfectly accurate for nanoridges in our sample. Nevertheless, the model is more suitable than the biaxial strain model, which assumes equal strain in both directions.

Using Equation 1, the strain difference between the ridge and the flat area was calculated to be $(1.6 \pm 0.5) \times 10^{-3}$. The positive value indicates that the strain on the ridges is less compressive than that in the flat area, which is concordant with the 'ridge as a compressive strain relaxation' mechanism.[5,9] It is interesting to compare this value with the TERS result of a nanoridge on large-sheet epitaxial graphene reported in our previous study. Despite the difference in the height of the nanoridge (~2 nm vs ~6 nm), this ridge-flat strain difference is almost equal to the value of $(1.6 \pm 0.2) \times 10^{-3}$ in our previous study.[9] This might be partly by chance, as the TERS results from some other ridges give significantly smaller values of strain difference (see Figure 4a). However, it does demonstrate that nanoridges on epitaxial graphene microislands also provide compressive strain relaxation of a similar order of magnitude to nanoridges on large-sheet epitaxial graphene. If the band position from far-field Raman spectra is used, then the calculated strain difference between the ridge and flat area would be just 7.21×10^{-5}, a value smaller than the uncertainty range. This means normal micro-Raman measurement does not have enough spatial resolution to detect ridge-flat strain difference, thus making TERS a necessity.

It is well-known that the SiC step/plateau acts as a graphene nucleation point. Then, at the edge of nucleated graphene, SiC decomposition releases Si vapour to the atmosphere and allows the remaining carbon atoms to contribute to graphene growth.[1,3] The graphene microisland in this study clearly grew from the center to the edge of the hexagonal island. The near-perfect equiangular shape of the island suggests that there is only one nucleation point in the center. This obvious growth pattern helps in the discussion of nanoridges formation. The alternative mechanism of nanoridges origin (i.e., the accumulation of trapped Si vapour),[41] is unlikely to occur in this sample because of three reasons: 1) SiC decomposition (and so Si sublimation) can only occur at the graphene edges as the island grows, and not in the center, otherwise there will be multiple layers formed. The Si vapour produced near the edges could easily escape out from the island, and thus cannot accumulate into nanoridge. 2) AFM images show that many nanoridges extend to the edge of the island, and these open cavities cannot trap Si vapour. The one among these ridges (Figure 3c and 4a, point number 3) gives a similar TERS spectrum to nanoridges on other position. 3) The island should have a poor capability to trap Si vapour due to its small size. Despite these reasons that the ‘Si vapour trapping’ mechanism cannot occur, nanoridges with compressive strain relaxation are still observed in the graphene microisland. This indicates that the ‘strain relaxation’ mechanism alone is enough to create nanoridges.

Aside from the peak position, the G′ band in the TERS spectrum from the ridge in

Figure 3d appears broader than that from the flat area. One possible explanation for the broadening is that nanoridges relax the strain in only one direction,[5] and thus the strain in the direction across the ridge is weaker than that along the ridge. Graphene with such a difference of strains between the two axes is known to exhibit a splitting of G and G′ band.[54,63,64] The degree of splitting depends on the strain difference. In the cases where this splitting is too small to be discerned, the bands appear instead as a broad band.[54,64] This possibility was confirmed by resolving the G′ band with two Lorentzian peaks. By fixing one peak at 2691 cm^{-1} (the average peak position of G′ band from the flat area), both of the resolved peaks have FWHM of 30 cm^{-1}, which is very close to FWHM in the far-field Raman spectra (Figure 3e). Since a FWHM of around 30 cm^{-1} is a well-known characteristic of single layer graphene, the FWHM values of the resolved peaks are important in confirming that the broadening does not arises from multi-layer graphene, but rather from strain inequality. The peak positions from the two-peak approach can be also calculated into new value of strain relaxations.

Figure 4a and 4b depict the greater variation of G′ band FWHM in the TERS spectra from the nanoridges, compared to the flat areas and to the far-field spectra from both areas. Based on the semi-splitting explanation in the previous paragraph, this indicates that the inequality of strain in the two axes is different among each nanoridge. These results demonstrate that TERS does not only reveal the inhomogeneity in the magnitude of the strain, but also in the direction of strain.

As in the case of graphene island edges, the TERS result shows no significant difference in graphene peaks positions and FWHMs from the TERS spectra of the flat areas inside the island. The D band is also absent in the TERS spectrum from the edge, which is similar to the far-field Raman spectra discussed in the previous section. This is expected because the growth of epitaxial graphene tends to minimize edge energy.[48] It is thermodynamically preferred to have a clear and smooth edge rather than an irregular edge in the nanoscale. However, this does not rule out the possibility of a small D band that is below the detection limit of the TERS experiment.

TERS mapping was impractical to be performed in this study due to the long exposure time required for each spectrum, which is a consequence of weak TERS signal. The inevitable reasons of the weak signal are: 1) gap mode enhancement using gold/silver substrate cannot be done for this sample, since SiC is already under the graphene. 2) Raman signal of graphene grown on SiC is weaker than exfoliated graphene on SiO_2, because of stronger substrate interaction. 3) non-contact mode tip controlling was required to prevent nanostructures deformations by the tips. The larger tip-sample distance compared to contact mode makes the enhancement lower, as the near field enhancement decay by distance from tip.[19]

Conclusion

Hexagonal epitaxial graphene microislands were synthesized by annealing pre-engraved 4H-SiC $(000\bar{1})$. The studied island was several micrometres in both height and width, consisted of a single layer of graphene throughout its sheet, and had no grain boundary. AFM analysis revealed nanoridges with a height of ∼2 nm all over the island. Although the island appeared homogeneous at the scale of micro-Raman imaging, TERS shows that nanoridges cause a nanoscale variation of strain in terms of both magnitude and direction. The G′ band shift of 9 cm-1 between the TERS spectra from a nanoridge and flat area can be calculated into a strain difference of (1.6 ± 0.5) × 10-3, indicating a relaxation of compressive strain on the ridge. The similar strain change that occurs in both graphene island and large sheet graphene suggests that the ‘compressive strain relaxation’ mechanism is sufficient for nanoridges to form, since the ‘Si vapour accumulation’ mechanism being unlikely to have occurred in this sample.

References

(1) Ouerghi, A.; Silly, M. G.; Marangolo, M.; Mathieu, C.; Eddrief, M.; Picher, M.; Sirotti, F.; El

Moussaoui, S.; Belkhou, R. Large-Area and High-Quality Epitaxial Graphene on Off-Axis SiC Wafers. *ACS Nano* **2012**, *6* (7), 6075–6082.

(2) Emtsev, K. V.; Bostwick, A.; Horn, K.; Jobst, J.; Kellogg, G. L.; Ley, L.; McChesney, J. L.; Ohta, T.; Reshanov, S. A.; Röhrl, J.; et al. Towards Wafer-Size Graphene Layers by Atmospheric Pressure Graphitization of Silicon Carbide. *Nat. Mater.* **2009**, *8* (3), 203–207.

(3) Ushio, S.; Kutsuma, Y.; Yoshii, A.; Tamai, N.; Ohtani, N.; Kaneko, T. 4H-SiC(0001) Basal Plane Stability during the Growth of Epitaxial Graphene on Inverted-Mesa Structures. *Jpn. J. Appl. Phys.* **2011**, *50* (7R), 070104.

(4) Velez-Fort, E.; Mathieu, C.; Pallecchi, E.; Pigneur, M.; Silly, M. G.; Belkhou, R.; Marangolo, M.; Shukla, A.; Sirotti, F.; Ouerghi, A. Epitaxial Graphene on 4H-SiC(0001) Grown under Nitrogen Flux: Evidence of Low Nitrogen Doping and High Charge Transfer. *ACS Nano* **2012**, *6* (12), 10893–10900.

(5) Prakash, G.; Capano, M. A.; Bolen, M. L.; Zemlyanov, D.; Reifenberger, R. G. AFM Study of Ridges in Few-Layer Epitaxial Graphene Grown on the Carbon-Face of 4H–SiC. *Carbon* **2010**, *48* (9), 2383–2393.

(6) Sun, G. F.; Jia, J. F.; Xue, Q. K.; Li, L. Atomic-Scale Imaging and Manipulation of Ridges on Epitaxial Graphene on 6H-SiC(0001). *Nanotechnology* **2009**, *20* (35), 355701.

(7) Xu, P.; Barber, S. D.; Schoelz, J. K.; Ackerman, M. L.; Qi, D.; Thibado, P. M.; Wheeler, V. D.; Nyakiti, L. O.; Myers-Ward, R. L.; Jr, C. R. E.; et al. Atomic-Scale Movement Induced in Nanoridges by Scanning Tunneling Microscopy on Epitaxial Graphene Grown on 4H-SiC(0001). *J. Vac. Sci. Technol. B* **2013**, *31* (4), 04D101.

(8) Wang, F.; Liu, G.; Rothwell, S.; Nevius, M.; Tejeda, A.; Taleb-Ibrahimi, A.; Feldman, L. C.; Cohen, P. I.; Conrad, E. H. Wide-Gap Semiconducting Graphene from Nitrogen-Seeded SiC. *Nano Lett.* **2013**, *13* (10), 4827–4832.

(9) Vantasin, S.; Tanabe, I.; Tanaka, Y.; Itoh, T.; Suzuki, T.; Kutsuma, Y.; Ashida, K.; Kaneko, T.; Ozaki, Y. Tip-Enhanced Raman Scattering of the Local Nanostructure of Epitaxial Graphene Grown on 4H-SiC (000$\bar{1}$). *J. Phys. Chem. C* **2014**, *118* (44), 25809–25815.

(10) Srivastava, N.; He, G.; Luxmi; Mende, P. C.; Feenstra, R. M.; Sun, Y. Graphene Formed on SiC under Various Environments: Comparison of Si-Face and C-Face. *J. Phys. Appl. Phys.* **2012**, *45* (15), 154001.

(11) Luxmi; Fisher, P. J.; Srivastava, N.; Feenstra, R. M.; Sun, Y.; Kedzierski, J.; Healey, P.; Gu, G. Morphology of Graphene on SiC(0001¯) Surfaces. *Appl. Phys. Lett.* **2009**, *95* (7), 073101.

(12) Low, T.; Guinea, F.; Katsnelson, M. I. Gaps Tunable by Electrostatic Gates in Strained Graphene. *Phys. Rev. B* **2011**, *83* (19), 195436.

(13) Phark, S.; Borme, J.; Vanegas, A. L.; Corbetta, M.; Sander, D.; Kirschner, J. Scanning Tunneling Spectroscopy of Epitaxial Graphene Nanoisland on Ir(111). *Nanoscale Res. Lett.* **2012**, *7* (1), 255.

(14) Hicks, J.; Tejeda, A.; Taleb-ibrahimi, A.; Nevius, M. S.; Wang, F.; Shepperd, K.; Palmer, J.; Bertran, F.; Le Fèvre, P.; Kunc, J.; et al. A Wide-Bandgap Metal-Semiconductor-Metal Nanostructure Made Entirely from Graphene. *Nat. Phys.* **2013**, *9* (1), 49–54.

(15) Weng, X.; Robinson, J. A.; Trumbull, K.; Cavalero, R.; Fanton, M. A.; Snyder, D. Structure of Few-Layer Epitaxial Graphene on 6H-SiC(0001) at Atomic Resolution. *Appl. Phys. Lett.* **2010**, *97* (20), 201905.

(16) Malard, L. M.; Pimenta, M. A.; Dresselhaus, G.; Dresselhaus, M. S. Raman Spectroscopy in Graphene. *Phys. Rep.* **2009**, *473* (5-6), 51–87.

(17) Ferrari, A. C.; Basko, D. M. Raman Spectroscopy as a Versatile Tool for Studying the Properties of Graphene. *Nat. Nanotechnol.* **2013**, *8* (4), 235–246.

(18) Saito, Y.; Verma, P.; Masui, K.; Inouye, Y.; Kawata, S. Nano-Scale Analysis of Graphene Layers by Tip-Enhanced near-Field Raman Spectroscopy. *J. Raman Spectrosc.* **2009**, *40* (10), 1434–1440.

(19) Hoffmann, G. G.; Xue, L.; Loos, J.; de With, G. High-Resolution Tip-Enhanced Raman Mapping. *Macromol. Symp.* **2011**, *305* (1), 26–42.

(20) Ghislandi, M.; Hoffmann, G. G.; Tkalya, E.; Xue, L.; With, G. D. Tip-Enhanced Raman Spectroscopy and Mapping of Graphene Sheets. *Appl. Spectrosc. Rev.* **2012**, *47* (5), 371–381.

(21) Das, A.; Pisana, S.; Chakraborty, B.; Piscanec, S.; Saha, S. K.; Waghmare, U. V.; Novoselov, K. S.; Krishnamurthy, H. R.; Geim, A. K.; Ferrari, A. C.; et al. Monitoring Dopants by Raman Scattering in an Electrochemically Top-Gated Graphene Transistor. *Nat. Nanotechnol.* **2008**, *3* (4), 210–215.

(22) Schmidt, D. A.; Ohta, T.; Beechem, T. E. Strain and Charge Carrier Coupling in Epitaxial Graphene. *Phys. Rev. B* **2011**, *84* (23), 235422.

(23) Bruna, M.; Ott, A. K.; Ijäs, M.; Yoon, D.; Sassi, U.; Ferrari, A. C. Doping Dependence of the Raman Spectrum of Defected Graphene. *ACS Nano* **2014**, *8* (7), 7432–7441.

(24) Ferralis, N. Probing Mechanical Properties of Graphene with Raman Spectroscopy. *J. Mater. Sci.*

2010, *45* (19), 5135–5149.

(25) Ferralis, N.; Maboudian, R.; Carraro, C. Evidence of Structural Strain in Epitaxial Graphene Layers on 6H-SiC(0001). *Phys. Rev. Lett.* **2008**, *101* (15), 156801.

(26) Cançado, L. G.; Jorio, A.; Ferreira, E. H. M.; Stavale, F.; Achete, C. A.; Capaz, R. B.; Moutinho, M. V. O.; Lombardo, A.; Kulmala, T. S.; Ferrari, A. C. Quantifying Defects in Graphene via Raman Spectroscopy at Different Excitation Energies. *Nano Lett.* **2011**, *11* (8), 3190–3196.

(27) Verma, P.; Ichimura, T.; Yano, T.; Saito, Y.; Kawata, S. Nano-Imaging through Tip-Enhanced Raman Spectroscopy: Stepping beyond the Classical Limits. *Laser Photonics Rev.* **2009**, *4* (4), 548–561.

(28) Domke, K. F.; Pettinger, B. Studying Surface Chemistry beyond the Diffraction Limit: 10 Years of TERS. *ChemPhysChem* **2010**, *11* (7), 1365–1373.

(29) Deckert, V. Tip-Enhanced Raman Spectroscopy. *J. Raman Spectrosc.* **2009**, *40* (10), 1336–1337.

(30) Hayazawa, N.; Inouye, Y.; Sekkat, Z.; Kawata, S. Metallized Tip Amplification of near-Field Raman Scattering. *Opt. Commun.* **2000**, *183* (1–4), 333–336.

(31) Kawata, S.; Inouye, Y.; Verma, P. Plasmonics for near-Field Nano-Imaging and Superlensing. *Nat. Photonics* **2009**, *3* (7), 388–394.

(32) Pashaee, F.; Sharifi, F.; Fanchini, G.; Lagugné-Labarthet, F. Tip-Enhanced Raman Spectroscopy of Graphene-like and Graphitic Platelets on Ultraflat Gold Nanoplates. *Phys. Chem. Chem. Phys.* **2015**, *17* (33), 21315–21322.

(33) Su, W.; Roy, D. Visualizing Graphene Edges Using Tip-Enhanced Raman Spectroscopy. *J. Vac. Sci. Technol. B* **2013**, *31* (4), 041808.

(34) Stadler, J.; Schmid, T.; Zenobi, R. Nanoscale Chemical Imaging of Single-Layer Graphene. *ACS Nano* **2011**, *5* (10), 8442–8448.

(35) Rickman, R. H.; Dunstan, P. R. Enhancement of Lattice Defect Signatures in Graphene and Ultrathin Graphite Using Tip-Enhanced Raman Spectroscopy: Enhancement of Defect Signatures in Graphene Using Tip-Enhanced Raman. *J. Raman Spectrosc.* **2014**, *45* (1), 15–21.

(36) Wang, P.; Zhang, D.; Li, L.; Li, Z.; Zhang, L.; Fang, Y. Reversible Defect in Graphene Investigated by Tip-Enhanced Raman Spectroscopy. *Plasmonics* **2012**, *7* (3), 555–561.

(37) Poliani, E.; Nippert, F.; Maultzsch, J. Effect of Gap Modes on Graphene and Multilayer Graphene in Tip-Enhanced Raman Spectroscopy. *Phys. Status Solidi B* **2012**, *249* (12), 2511–2514.

(38) Domke, K. F.; Pettinger, B. Tip-Enhanced Raman Spectroscopy of 6H-SiC with Graphene Adlayers: Selective Suppression of E1 Modes. *J. Raman Spectrosc.* **2009**, *40* (10), 1427–1433.

(39) Snitka, V.; Rodrigues, R. D.; Lendraitis, V. Novel Gold Cantilever for Nano-Raman Spectroscopy of Graphene. *Microelectron. Eng.* **2011**, *88* (8), 2759–2762.

(40) Suzuki, T.; Itoh, T.; Vantasin, S.; Minami, S.; Kutsuma, Y.; Ashida, K.; Kaneko, T.; Morisawa, Y.; Miura, T.; Ozaki, Y. Tip-Enhanced Raman Spectroscopic Measurement of Stress Change in the Local Domain of Epitaxial Graphene on the Carbon Face of 4H-SiC(0001¯). *Phys. Chem. Chem. Phys.* **2014**, *16* (37), 20236–20240.

(41) Hu, T. W.; Ma, D. Y.; Ma, F.; Xu, K. W. Preferred Armchair Edges of Epitaxial Graphene on 6H-SiC(0001) by Thermal Decomposition. *Appl. Phys. Lett.* **2012**, *101* (24), 241903.

(42) Wang, F.; Shepperd, K.; Hicks, J.; Nevius, M. S.; Tinkey, H.; Tejeda, A.; Taleb-Ibrahimi, A.; Bertran, F.; Le Fèvre, P.; Torrance, D. B.; et al. Silicon Intercalation into the Graphene-SiC Interface. *Phys. Rev. B* **2012**, *85* (16), 165449.

(43) Silly, M. G.; Li, G.; Dappe, Y. J. Electronic Properties of Zero-Layer Graphene on 6H-SiC(0001) Substrate Decoupled by Silicon Intercalation. *Surf. Interface Anal.* **2014**, *46* (12-13), 1273–1277.

(44) Silly, M. G.; D'Angelo, M.; Besson, A.; Dappe, Y. J.; Kubsky, S.; Li, G.; Nicolas, F.; Pierucci, D.; Thomasset, M. Electronic and Structural Properties of Graphene-Based Metal-Semiconducting Heterostructures Engineered by Silicon Intercalation. *Carbon* **2014**, *76*, 27–39.

(45) Trabelsi, A. B. G.; Ouerghi, A.; Kusmartseva, O. E.; Kusmartsev, F. V.; Oueslati, M. Raman Spectroscopy of Four Epitaxial Graphene Layers: Macro-Island Grown on 4H-SiC Substrate and an Associated Strain Distribution. *Thin Solid Films* **2013**, *539*, 377–383.

(46) Tedesco, J. L.; Jernigan, G. G.; Culbertson, J. C.; Hite, J. K.; Yang, Y.; Daniels, K. M.; Myers-Ward, R. L.; Jr, C. R. E.; Robinson, J. A.; Trumbull, K. A.; et al. Morphology Characterization of Argon-Mediated Epitaxial Graphene on C-Face SiC. *Appl. Phys. Lett.* **2010**, *96* (22), 222103.

(47) Manjavacas, A.; Thongrattanasiri, S.; de, A. F. J. G. Plasmons Driven by Single Electrons in Graphene Nanoislands. *Nanophotonics* **2013**, *2* (2), 139–151.

(48) Rutter, G. M.; Guisinger, N. P.; Crain, J. N.; First, P. N.; Stroscio, J. A. Edge Structure of Epitaxial Graphene Islands. *Phys. Rev. B* **2010**, *81* (24), 245408.

(49) Biedermann, L. B.; Bolen, M. L.; Capano, M. A.; Zemlyanov, D.; Reifenberger, R. G. Insights into Few-Layer Epitaxial Graphene Growth on 4H-SiC(0001¯) Substrates from STM Studies. *Phys. Rev. B* **2009**, *79* (12), 125411.

(50) Yue, Y.; Zhang, J.; Wang, X. Micro/Nanoscale Spatial Resolution Temperature Probing for the Interfacial Thermal Characterization of Epitaxial Graphene on 4H-SiC. *Small* **2011**, *7* (23), 3324–3333.

(51) Jiang, J.-W.; Wang, J.-S.; Li, B. Thermal Expansion in Single-Walled Carbon Nanotubes and Graphene: Nonequilibrium Green's Function Approach. *Phys. Rev. B* **2009**, *80* (20), 205429.

(52) Yoon, D.; Son, Y.-W.; Cheong, H. Negative Thermal Expansion Coefficient of Graphene Measured by Raman Spectroscopy. *Nano Lett.* **2011**, *11* (8), 3227–3231.

(53) Frank, O.; Tsoukleri, G.; Parthenios, J.; Papagelis, K.; Riaz, I.; Jalil, R.; Novoselov, K. S.; Galiotis, C. Compression Behavior of Single-Layer Graphenes. *ACS Nano* **2010**, *4* (6), 3131–3138.

(54) Mohiuddin, T. M. G.; Lombardo, A.; Nair, R. R.; Bonetti, A.; Savini, G.; Jalil, R.; Bonini, N.; Basko, D. M.; Galiotis, C.; Marzari, N.; et al. Uniaxial Strain in Graphene by Raman Spectroscopy: G Peak Splitting, Grüneisen Parameters, and Sample Orientation. *Phys. Rev. B* **2009**, *79* (20), 205433.

(55) Huang, M.; Yan, H.; Heinz, T. F.; Hone, J. Probing Strain-Induced Electronic Structure Change in Graphene by Raman Spectroscopy. *Nano Lett.* **2010**, *10* (10), 4074–4079.

(56) Ferralis, N.; Kawasaki, J.; Maboudian, R.; Carraro, C. Evolution in Surface Morphology of Epitaxial Graphene Layers on SiC Induced by Controlled Structural Strain. *Appl. Phys. Lett.* **2008**, *93* (19), 191916–191916 – 3.

(57) Bissett, M. A.; Tsuji, M.; Ago, H. Mechanical Strain of Chemically Functionalized Chemical Vapor Deposition Grown Graphene. *J. Phys. Chem. C* **2013**, *117* (6), 3152–3159.

(58) Pisana, S.; Lazzeri, M.; Casiraghi, C.; Novoselov, K. S.; Geim, A. K.; Ferrari, A. C.; Mauri, F. Breakdown of the Adiabatic Born–Oppenheimer Approximation in Graphene. *Nat. Mater.* **2007**, *6* (3), 198–201.

(59) Krauss, B.; Nemes-Incze, P.; Skakalova, V.; Biro, L. P.; Klitzing, K. von; Smet, J. H. Raman Scattering at Pure Graphene Zigzag Edges. *Nano Lett.* **2010**, *10* (11), 4544–4548.

(60) Guisinger, N. P.; Rutter, G. M.; Crain, J. N.; First, P. N.; Stroscio, J. A. Exposure of Epitaxial Graphene on SiC(0001) to Atomic Hydrogen. *Nano Lett.* **2009**, *9* (4), 1462–1466.

(61) Berciaud, S.; Ryu, S.; Brus, L. E.; Heinz, T. F. Probing the Intrinsic Properties of Exfoliated Graphene: Raman Spectroscopy of Free-Standing Monolayers. *Nano Lett.* **2009**, *9* (1), 346–352.

(62) Luo, X.; Goel, S.; Reuben, R. L. A Quantitative Assessment of Nanometric Machinability of Major Polytypes of Single Crystal Silicon Carbide. *J. Eur. Ceram. Soc.* **2012**, *32* (12), 3423–3434.

(63) Cheng, Y. C.; Zhu, Z. Y.; Huang, G. S.; Schwingenschlögl, U. Grüneisen Parameter of the G Mode of Strained Monolayer Graphene. *Phys. Rev. B* **2011**, *83* (11), 115449.

(64) Frank, O.; Mohr, M.; Maultzsch, J.; Thomsen, C.; Riaz, I.; Jalil, R.; Novoselov, K. S.; Tsoukleri, G.; Parthenios, J.; Papagelis, K.; et al. Raman 2D-Band Splitting in Graphene: Theory and Experiment. *ACS Nano* **2011**, *5* (3), 2231–2239.

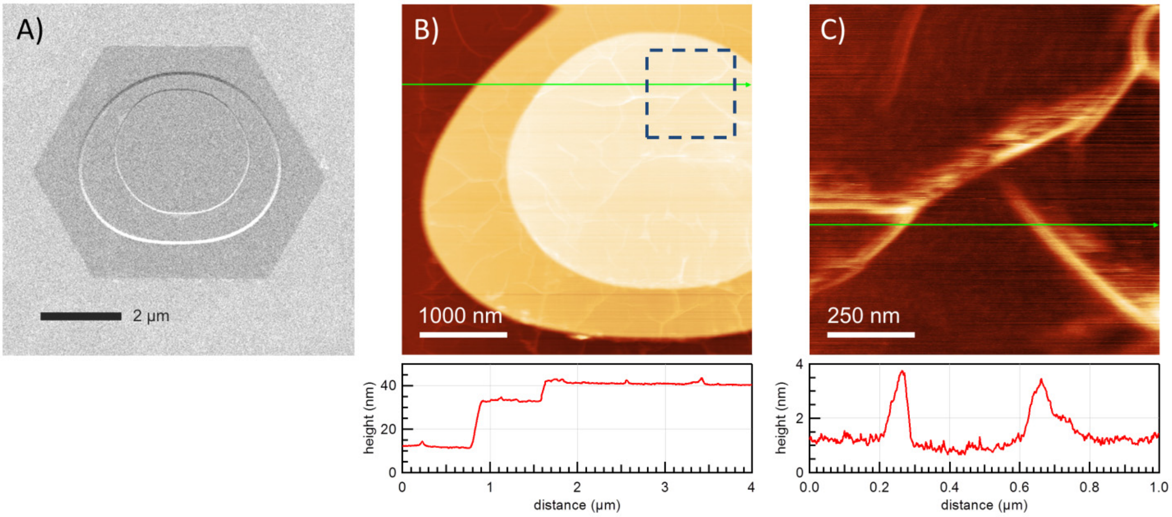

Figure 1 A) semi-low energy SEM image of a graphene microisland. B) AFM topography image of the graphene. C) Another AFM image on the smaller area of blue dashed square in B).

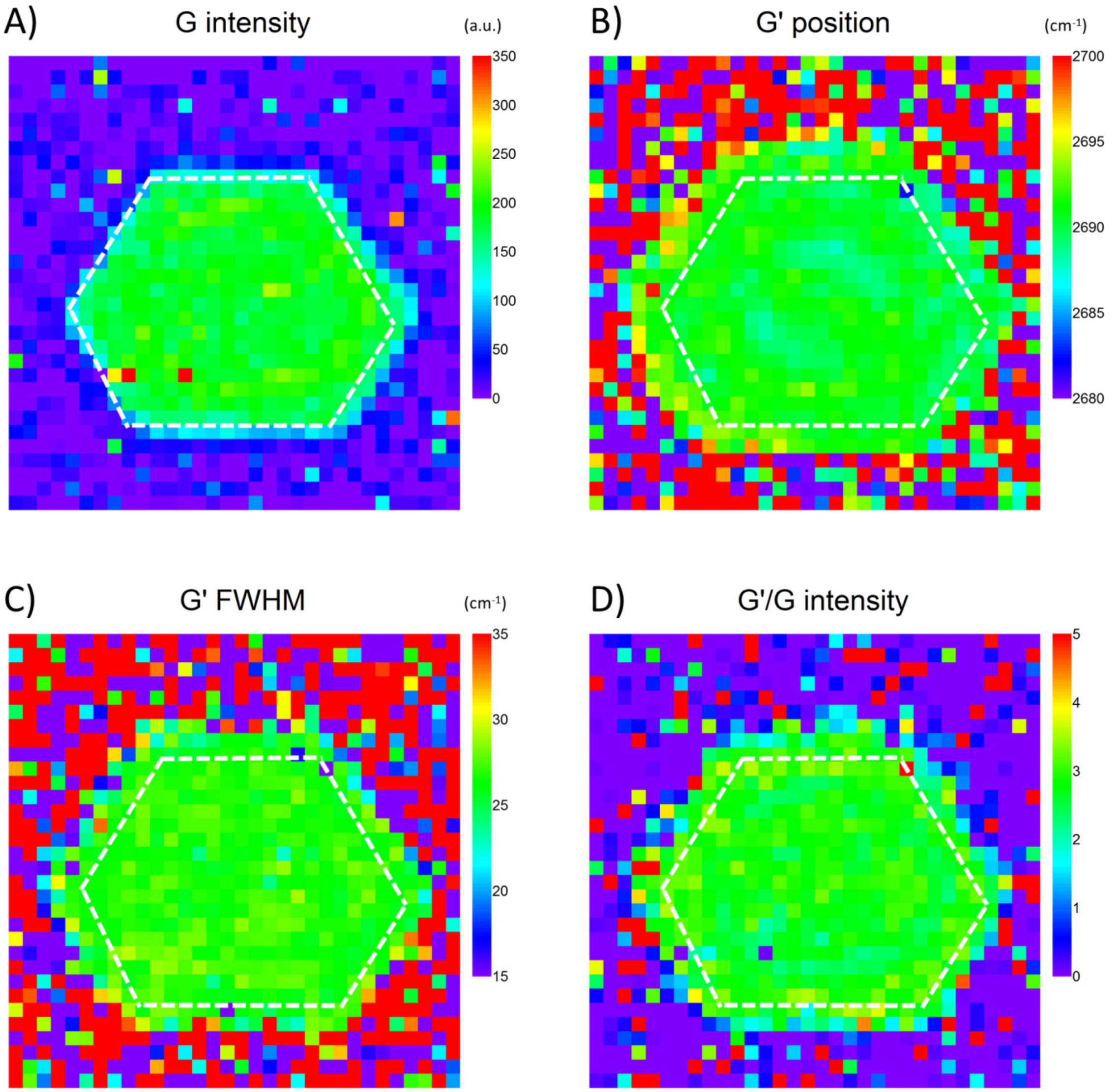

Figure 2 Raman imaging of the graphene microisland. The maps are 9.6 x 9.6 μm. Each map contains 32 x 32 spectra. The band intensities, positions, and FWHM are acquired by Lorentzian fitting.

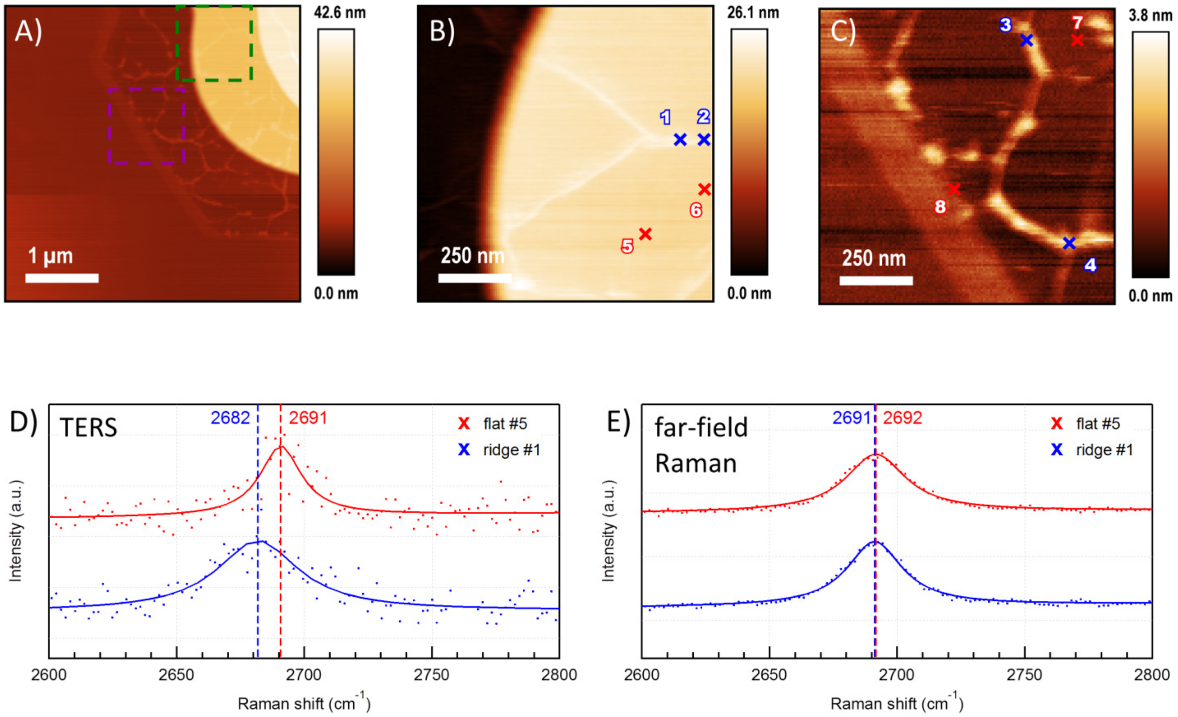

Figure 3 A) AFM topography image on the lower-left area of the island shown in Figure 1. B), C) Smaller area scans on green and purple dashed square in A). These AFM images are acquired using silicon AFM tips. Noted that the colour scale of A) is different from B) and C) due to an adjustment to increase the contrast for lower heights. D), E) G′ band in TERS and far-field spectra from flat and ridge at the position of X mark number 1 and 5 in B).

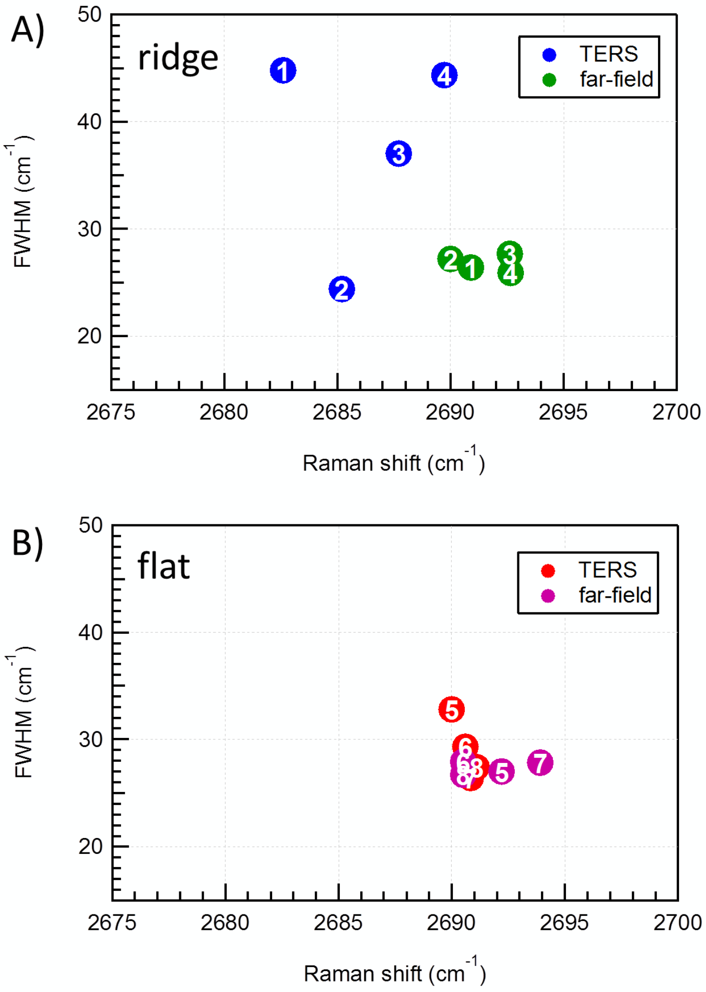

Figure 4 FWHM vs peak position of G′ band in TERS spectra from A) ridges and B) flat areas of the corresponding number marks in Figure 3B and 3C.

Chapter III: 3D SERS imaging using chemically-synthesized highly-symmetric nanoporous silver microstructure

Abstract

A synthesis, 3D SERS characterization, and potential applications of 3D highly-symmetric nanoporous silver microparticles have been demonstrated. The synthesis is chemical-based and capable for large-scale. Both of the particle shape and SERS enhancement pattern in 3D are very predictable, as they have regular hexapod shape with octahedral symmetry. By embedding the particles into polymer, 3D SERS imaging can reveal an inhomogeneity in the system which cannot be resolved by conventional 3D Raman imaging.

Introduction, result, and discussion

Surface-enhanced Raman scattering (SERS) spectroscopy, a highly sensitive and selective technique which provides rich molecular information, has been widely used in various applications including life sciences and materials sciences.[1–5] Recently, SERS substrates with three dimensions have been developed by many research groups and have been demonstrated to have promising signal quality due to their exponentially large surface area and large amount of hotspots from the additional third dimension.[6–8] However, almost all of the 3D SERS substrate studies demonstrated only point-by-point measurement or 2D SERS imaging, which does not fully utilize the three-dimensionality of the substrates. To the best of our knowledge, only one research[9] showed a breakthrough of 2D limitation with 3D SERS imaging on 3D SERS substrate and reported very interesting potential applications such as 3D-encoding of digital data. Even so, the research used lithography-base synthesis of the SERS substrate, which makes the enhancing surface being topologically extruded 2D plane rather than a proper 3D object. It is worthy to note that there are the uses of nanoparticles aggregates[10,11] or 3D-movement nanoparticle tracking[12] to do 3D SERS imaging in cells, which allow amazing investigations of intracellular pathway, but have a limited application in materials science since the aggregation and 3D motion of nanoparticle are semi-random, and thus enhancement pattern is unpredictable. The present study tries to use chemically-synthesized symmetric silver microparticles to further push the potential of 3D SERS imaging with the novel 3D SERS substrate into creative applications such as dispersible embedding 3D SERS probe, which allows the use of much lower laser power compared to normal Raman spectroscopy, but providing an improved spatial resolution. The objective is not to claim the superiority in an enhancement factor over the previously reported substrates, but to provide an alternative substrate for unexplored applications.

Nanoporous silver microstructures in this study were synthesized by in-place galvanic reduction of AgCl template as described in Experimental Section. A SEM image in Figure 1A shows a regular hexapod shape with octahedral symmetry (each leg has the same length and is 90° from the adjacent.). The nanopores which would acts as hotspots are presented in Figure 1B, with an average pore size of ~60 nm. This pore size should allow small molecules, such as SERS probe molecules, to go deep inside cavities of the particles, instead of just the outer surface. Its Raman enhancement uniformity in a single microstructure was evaluated to be within an order of magnitude by our previous study.[13] The study also confirmed the 99.9 % purity of silver throughout the structures by energy-dispersive X-ray spectroscopy (EDS).

An advantage of octahedral symmetric shape is that when the silver microparticles lie on a flat surface, no matter what the direction is, they would always be pulled down by gravity and rest on three legs, with the other three legs pointing upward 45° from the flat surface plane, as shown in Figure 1A. Due to the symmetry, every hexapod particle would have an apparent leg-to-adjacent-leg angle and leg-to-opposite-leg size of 30° and 2cos(leg-length), respectively, viewing from the Z axis (and from all direction equivalent to the Z axis in octahedral symmetry). The particle orientation similar to Figure 1A almost always happens for a hexapod-shape particle, and thus it is an easy-to-find target. The capability that lower legs can be seen from the top together with the upper legs is also an important factor which allows 3D SERS imaging.

Figure 2A shows a SERS spectrum of p-aminothiophenol (PATP) from the center of the particle in Figure 2B. PATP is a well-known and important SERS probe because it can adsorb very well on silver, giving strong SERS signal.[14–17] In our previous study, PATP with a concentration as low as 10^{-8} M could be detected by SERS with similar hexapod silver microstructures.[13] Figure 2C, D, and E display 3D SERS imaging from simple area integration of the 1075 cm^{-1} band. Each image represents volumetric data of 45 × 45 × 45 spectra spanning in the XYZ space of 13.2^3 μm^3 (see Experimental Section). The band was selected because it is a simple Raman band which can be unambiguously assigned to a_1 mode C-S stretching of PATP in C_{2V} point group.[14,16,18] The enhancement pattern is easily predictable, as the top-view enhancement mapping in Figure 2C closely resembles the particle shape in Figure 2B. The XY-slices shown in Figure 2E also show an obvious pattern, as the hotspots are gradually translated from upper leg positions to lower leg positions. Both Figure 2D and 2E indicate that the SERS enhancements appear to be slightly lesser for the lower legs than the upper legs. This is most likely due to the shadowing effect, as the upper legs block some part of incoming excitation laser and scattered signal from the lower legs. This hypothesis can be carried out by doing 3D SERS imaging on many hexapod particles, as all particles measured show similar trends in upper leg/lower leg signal. (See supporting information.) The symmetry and regularity in the structure, along with the predictable enhancement pattern of this 3D SERS substrate is crucial in sensing application; if there are irregular or large difference in SERS signal from each equivalent leg of the hexapod, it is certain that the difference comes from external factors (e.g. sample inhomogeneity), not the particle itself.

Polarization of excitation laser can have huge impact in Raman enhancement for nanostructure-based SERS substrates.[19,20] Thus, it is of particular interest to study the effect of polarization on the 3D enhancement pattern. In Figure S1 of supporting information, 3D SERS images using the excitation laser with 0°, 45°, and 90° polarizations are presented (using the same particle as that in Figure 2). Figure S1A, B, and C illustrates top-view images obtained by using the 1074 cm^{-1} band area. Figure S1D, E, and F presents the corresponding side-view images. It is clear that there is only subtle change in the enhancement pattern for this Raman band among the three polarizations. The electromagnetic enhancement of nanostructured silver is a nanoscale phenomenon, and therefore, it does not affect the outline shape of this micrometers-scale enhancement pattern, which is dictated by the particle shape. Moreover, the inner nanoscale pattern is also unaffected. In the maps of 1074 cm^{-1} peak area shown in Figure 1S A-F, one can see that some areas with red/bright color indicating higher enhancement, and that these areas are similar for all polarizations. This indicates uniform distribution of the nanopores (no special nano-orientation). The polarization independence of enhancement pattern of the simple Raman band is useful, since it also means that there is no complication from the rotation of the particles in the XY plane.

A possible application of this 3D substrate is demonstrated by embedding the microparticle into polymers. Since this substrate has inherent SERS activity from its uniform nanopores and does not need either nanoparticle-decoration or aggregation, there is no risk of enhancement loss by the detachment of nanoparticles. Therefore, one may embed it in various environments while keeping its SERS activity. Contrary to the plane-extruding lithography-type 3D substrates, which are bound to the underlying surface, this substrate can go anywhere in the sample, even the volume near the top of the sample. For example, the upper legs of the silver hexapod in Figure 3A are located around 3 μm under the polymer surface and the particle bottom is still several micrometers over underneath glass slide. In this experiment 1:1 poly(3-hydroxybutyrate) (PHB)/poly(D,L)lactic acid (PDLLA) blend was used. Both polymers are popular biodegradable polymers, and blending them together improves physical properties over the original polymers.[21–23] This blend was chosen because the two polymers have the same functional groups (ester carbonyl and methyl groups), but are enough different in their Raman spectra. (See structure in supporting information Figure S2.) Due to the same functional groups, the interaction of each polymer to silver should be very similar and differences in the measured SERS spectra should come from the different in polymer distribution.

Figure 3B presents a top-view SERS image of the 3D imaging on the particle shown in Figure 3A, with the color representing the ratio of 870/840 cm^{-1} peak areas (from the 855-885 cm^{-1} and 830-850 cm^{-1} integral ranges, respectively). The peaks are originated from C-COO stretching modes of PDLLA and PHB,[21] respectively. The three example spectra from the 3D imaging are shown in Figure S3 of Supporting Information. The enhancement is actually very low compared to PATP because the carbonyl group of polymers does not adsorb very well on the silver particle. Nevertheless, the 3D image based the on peak area ratio shows a high value in some nanoscale area, which could be interpreted into an inhomogeneity of the blend (in which the area consists of more PDLLA content). Actually, the use of normal 3D Raman imaging to probe the inhomogeneity in polymers have been demonstrated,[24,25] but it is well-known that Raman spectroscopy in polymers suffers from a limitation in spatial resolution due to refraction, especially in the Z-axis.[26,27] It can be clearly seen in the 3D Raman images of the nearby polymer without silver structure (Figure 3C and 3E), that the inhomogeneity is not resolved very well. With the symmetric 3D SERS substrate as a near-field probe, the shape of the substrate constrains the probing area, and thus the small inhomogeneity can be resolved.

The capability in improving the spatial resolution in the Z axis can be demonstrated in the two-layer polymer systems. Hexapod silver particles were embedded into the interface between polyvinylpyrrolidone (PVP) and polystyrene (PS) (Figure 4A-B). Similar to the polymer blend system, the low enhancement from the poor adsorption resulting in noisy 3D SERS images. Nevertheless, using the peak area ratio between PS ring-mode vibration[28] (1002 cm^{-1}) and PVP C-C ring breathing[29] (933 cm^{-1}), the partition of the polymers can be seen. A top-view 3D SERS image in Figure 4C shows red color on upper legs of the particle, indicating high PS peak area, while lower legs exhibit low value of the ratio, representing

PVP. With the side-view 3D SERS image and median peak area ratio at the specific heights (Figure 4D-E), one can see that the ratio transition from the PS-like into PVP-like in just around 1 μm, contrary to a few micrometers in normal 3D Raman imaging.

Using 3D SERS imaging, we characterized the highly-symmetric nonporous silver microparticles about its SERS activities in three dimensions. The result showed that the substrate can provide volumetric SERS information. The enhancement pattern of particles is very predictable as it correlates well with the particle shape. The polarization-independent enhancement pattern is an advantage, as it allows the substrate to be useful in every orientation. A potential application as an embedding SERS probe was demonstrated. In a PHB/PDLLA polymery blend, 3D SERS imaging on this symmetric nonporous silver structure can resolve a small inhomogeneity of the blends. An improved spatial resolution in the Z axis was also illustrated by two-layer polymer system.

Experimental Section

Nanoporous silver microparticles with 3D symmetry were chemically synthesized by in-place galvanic reduction of 3D AgCl particles. The method is slightly modified from that reported in our previous study.[13,30] $AgNO_3$ (0.1 M, 5 mL) and NH_4OH (5.31 M, 4.7 mL) were thoroughly mixed, and then the solution was quickly added into excess amount of vigorously stirred 1 M NaCl solution. White AgCl precipitates were formed immediately after the mixing, but the stirring is kept for 5 minutes in ambient conditions. The AgCl particles was washed with water and ethanol, dried in air, and reduced with a Zn plate in NaCl solution (0.1 M, 50 mL) until AgCl microparticles were completely converted to nanoporous hexapod silver microparticles. (The color of particles changed from white to dark grey.) Since the process does not involve lithography, it is highly scalable to the scale of several grams.

In the sample preparation for SERS of PATP experiment, one milligram of silver microparticles were washed a few times with water and ethanol (sonicated until disperse in water or ethanol, centrifuge, and then remove the liquid part). The particles were then mixed with 10^{-3} M PATP for one hour. The mixture was dropped onto a glass slide, and then washed with ethanol to remove non-adsorbed PATP.

3D SERS measurement was carried out with a Renishaw Invia Raman spectrometer equipped with a 532 nm solid-state laser. The objective lens used had 100X magnification and 0.85 NA (Leica N PLAN). The measurement was done by moving the sample with an automated XYZ stage controller and then SERS spectra were acquired point-by-point to get multiple spectra in 3D Cartesian grid. Every 3D SERS images in Figure 2 and 3 contains 45 × 45 × 45 points, with 0.3 µm separation between points and 0.4 s exposure time per point. The laser power was only 0.010 mW to prevent silver nanostructure from nanoscale deformation. The 3D images were generated using volume rendering (Bunyk ray cast) of Paraview 4.4.0. The optical images in Figure 2B and 4A were from focus-stacking technique, which is a merging of multiple images taken in the same position but different focus. Picolay software was used to merge the images.

For the polymer-embedded experiment, washed silver microparticles were dried with a vacuum oven (50 °C, -28 inHg relative to ambient pressure). After that, the particles were dispersed in chloroform with ratio of ~2 mg particle per 1 mL of chloroform. The 0.250 mL of the mixture was then mixed with 0.45 mL of 0.5 % PHB/0.5 % PDLLA blend in chloroform. This silver/particle mixture was dropped on a glass slide. Three drops were overlapped to build up the film with various thicknesses, which allows silver particles that are fully covered with polymer to be found. The procedure of 3D SERS measurement was the same as previous paragraph but with 35 × 35 × 35 points and 1 s exposure time. The point separation in the Z axis was reduced to 0.2 µm to compensate the higher refractive index of polymer compared to air. (Objects inside the polymer appear shallower.) For 3D Raman mapping without the SERS substrate in Figure 3C, laser power had to be as high as 5 mW, because normal Raman provided much lower signal than SERS.

The two-layer polymer sample was prepared by casting 0.500 mL of 1.25 % PVP together with 1 mg of silver particles. The microscope of Renishaw Invia was use to spot particles which are covered by PVP for around a half of their heights. 0.300 mL of 1 % PS in 2-butanone was then cast over the sample at 50 °C. The 3D imaging then performed on previously spotted particle with the same condition as the previous paragraph, but with 41 × 41 × 41 points.

References

(1) *Surface-Enhanced Raman Scattering*; Kneipp, K., Moskovits, M., Kneipp, H., Eds.; Topics in Applied Physics; Springer Berlin Heidelberg, 2006; Vol. 103.

(2) Aroca, R. *Surface-Enhanced Vibrational Spectroscopy: Aroca/Surface-Enhanced Vibrational Spectroscopy*; John Wiley & Sons, Ltd: Chichester, UK, 2006.

(3) *Frontiers of Surface-Enhanced Raman Scattering: Single-Nanoparticles and Single Cells*; Ozaki, Y., Kneipp, K., Aroca, R., Eds.; John Wiley & Sons, Inc: Chichester, West Sussex, 2014.

(4) McNay, G.; Eustace, D.; Smith, W. E.; Faulds, K.; Graham, D. Surface-Enhanced Raman Scattering (SERS) and Surface-Enhanced Resonance Raman Scattering (SERRS): A Review of Applications. *Appl. Spectrosc.* **2011**, *65* (8), 825–837.

(5) Hering, K.; Cialla, D.; Ackermann, K.; Dörfer, T.; Möller, R.; Schneidewind, H.; Mattheis, R.; Fritzsche, W.; Rösch, P.; Popp, J. SERS: A Versatile Tool in Chemical and Biochemical Diagnostics. *Anal. Bioanal. Chem.* **2007**, *390* (1), 113–124.

(6) Tang, H.; Meng, G.; Huang, Q.; Zhang, Z.; Huang, Z.; Zhu, C. Arrays of Cone-Shaped ZnO Nanorods Decorated with Ag Nanoparticles as 3D Surface-Enhanced Raman Scattering Substrates for Rapid Detection of Trace Polychlorinated Biphenyls. *Adv. Funct. Mater.* **2012**, *22* (1), 218–224.

(7) Lee, S. Y.; Kim, S.-H.; Kim, M. P.; Jeon, H. C.; Kang, H.; Kim, H. J.; Kim, B. J.; Yang, S.-M. Freestanding and Arrayed Nanoporous Microcylinders for Highly Active 3D SERS Substrate. *Chem. Mater.* **2013**, *25* (12), 2421–2426.

(8) Ko, H.; Singamaneni, S.; Tsukruk, V. V. Nanostructured Surfaces and Assemblies as SERS Media. *Small* **2008**, *4* (10), 1576–1599.

(9) Zhang, Q.; Lee, Y. H.; Phang, I. Y.; Lee, C. K.; Ling, X. Y. Hierarchical 3D SERS Substrates Fabricated by Integrating Photolithographic Microstructures and Self-Assembly of Silver Nanoparticles. *Small* **2014**, *10* (13), 2703–2711.

(10) McAughtrie, S.; Lau, K.; Faulds, K.; Graham, D. 3D Optical Imaging of Multiple SERS Nanotags in Cells. *Chem. Sci.* **2013**, *4* (9), 3566.

(11) Huefner, A.; Septiadi, D.; Wilts, B. D.; Patel, I. I.; Kuan, W.-L.; Fragniere, A.; Barker, R. A.; Mahajan, S. Gold Nanoparticles Explore Cells: Cellular Uptake and Their Use as Intracellular Probes. *Methods* **2014**, *68* (2), 354–363.

(12) Huang, K.-C.; Bando, K.; Ando, J.; Smith, N. I.; Fujita, K.; Kawata, S. 3D SERS (surface Enhanced Raman Scattering) Imaging of Intracellular Pathways. *Methods* **2014**, *68* (2), 348–353.

(13) Wongravee, K.; Gatemala, H.; Thammacharoen, C.; Ekgasit, S.; Vantasin, S.; Tanabe, I.; Ozaki, Y. Nanoporous Silver Microstructure for Single Particle Surface-Enhanced Raman Scattering Spectroscopy. *RSC Adv* **2015**, *5* (2), 1391–1397.

(14) Wu, D.-Y.; Liu, X.-M.; Huang, Y.-F.; Ren, B.; Xu, X.; Tian, Z.-Q. Surface Catalytic Coupling Reaction of P-Mercaptoaniline Linking to Silver Nanostructures Responsible for Abnormal SERS Enhancement: A DFT Study. *J. Phys. Chem. C* **2009**, *113* (42), 18212–18222.

(15) Huang, Y.-F.; Zhu, H.-P.; Liu, G.-K.; Wu, D.-Y.; Ren, B.; Tian, Z.-Q. When the Signal Is Not from the Original Molecule To Be Detected: Chemical Transformation of Para-Aminothiophenol on Ag during the SERS Measurement. *J. Am. Chem. Soc.* **2010**, *132* (27), 9244–9246.

(16) Osawa, M.; Matsuda, N.; Yoshii, K.; Uchida, I. Charge Transfer Resonance Raman Process in Surface-Enhanced Raman Scattering from P-Aminothiophenol Adsorbed on Silver: Herzberg-Teller Contribution. *J. Phys. Chem.* **1994**, *98* (48), 12702–12707.

(17) Kim, K.; Kim, K. L.; Shin, D.; Choi, J.-Y.; Shin, K. S. Surface-Enhanced Raman Scattering of 4-Aminobenzenethiol on Ag and Au: pH Dependence of b2-Type Bands. *J. Phys. Chem. C* **2012**, *116* (7), 4774–4779.

(18) Wang, Y.; Ji, W.; Yu, Z.; Li, R.; Wang, X.; Song, W.; Ruan, W.; Zhao, B.; Ozaki, Y. Contribution of Hydrogen Bonding to Charge-Transfer Induced Surface-Enhanced Raman Scattering of an

Intermolecular System Comprising P-Aminothiophenol and Benzoic Acid. *Phys. Chem. Chem. Phys.* **2014**, *16* (7), 3153–3161.

(19) Shegai, T.; Li, Z.; Dadosh, T.; Zhang, Z.; Xu, H.; Haran, G. Managing Light Polarization via Plasmon–molecule Interactions within an Asymmetric Metal Nanoparticle Trimer. *Proc. Natl. Acad. Sci.* **2008**, *105* (43), 16448–16453.

(20) Steinigeweg, D.; Schütz, M.; Schlücker, S. Single Gold Trimers and 3D Superstructures Exhibit a Polarization-Independent SERS Response. *Nanoscale* **2012**, *5* (1), 110–113.

(21) Furukawa, T.; Sato, H.; Murakami, R.; Zhang, J.; Noda, I.; Ochiai, S.; Ozaki, Y. Raman Microspectroscopy Study of Structure, Dispersibility, and Crystallinity of Poly(hydroxybutyrate)/poly(l-Lactic Acid) Blends. *Polymer* **2006**, *47* (9), 3132–3140.

(22) Meaurio, E.; Zuza, E.; Sarasua, J.-R. Direct Measurement of the Enthalpy of Mixing in Miscible Blends of Poly(dl-Lactide) with Poly(vinylphenol). *Macromolecules* **2005**, *38* (22), 9221–9228.

(23) Dong, W.; Ma, P.; Wang, S.; Chen, M.; Cai, X.; Zhang, Y. Effect of Partial Crosslinking on Morphology and Properties of the Poly(β-Hydroxybutyrate)/poly(d,l-Lactic Acid) Blends. *Polym. Degrad. Stab.* **2013**, *98* (9), 1549–1555.

(24) Smitthipong, W.; Gadiou, R.; Vidal, L.; Wagner, P.; Nardin, M. 3D Raman Images of Rubber Blends (IR–HNBR). *Vib. Spectrosc.* **2008**, *46* (1), 8–13.

(25) Larsen, R. A.; Kubo, Y.; Akao, K.; Ohkubo, Y.; Yumoto, M.; Nagoshi, T. Raman Spectral Imaging—Expanding Capabilities to Fulfill Application Requirements. In *AIP Conference Proceedings*; AIP Publishing, 2010; Vol. 1267, pp 766–767.

(26) Everall, N. J. Confocal Raman Microscopy: Why the Depth Resolution and Spatial Accuracy Can Be Much Worse than You Think. *Appl. Spectrosc.* **2000**, *54* (10), 1515–1520.

(27) Everall, N. J. Modeling and Measuring the Effect of Refraction on the Depth Resolution of Confocal Raman Microscopy. *Appl. Spectrosc.* **2000**, *54* (6), 773–782.

(28) Lobo, H.; Bonilla, J. V. *Handbook of Plastics Analysis*; CRC Press, 2003.

(29) Taylor, L. S.; Langkilde, F. W.; Zografi, G. Fourier Transform Raman Spectroscopic Study of the Interaction of Water Vapor with Amorphous Polymers. *J. Pharm. Sci.* **2001**, *90* (7), 888–901.

(30) Gatemala, H.; Thammacharoen, C.; Ekgasit, S. 3D AgCl Microstructures Selectively Fabricated via Cl−-Induced Precipitation from [Ag(NH3)2]+. *CrystEngComm* **2014**, *16* (29), 6688.

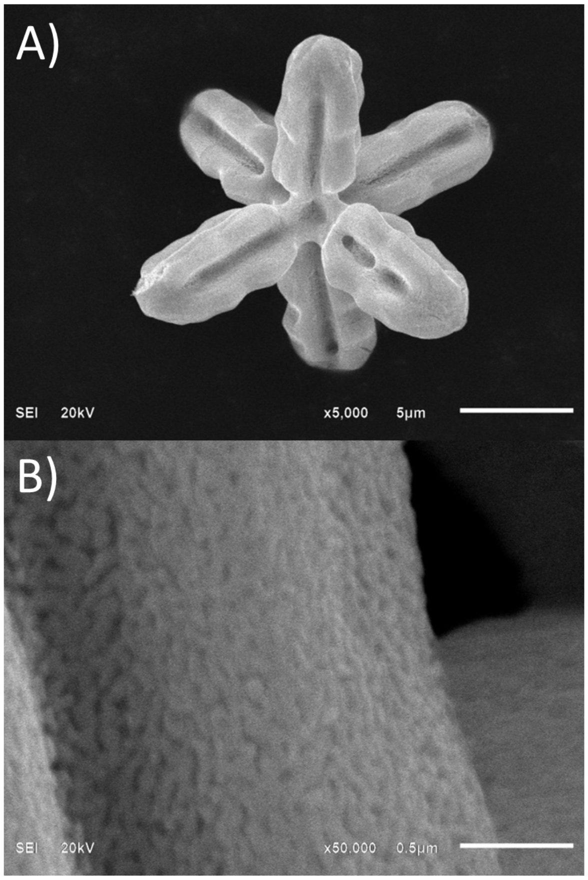

Figure 1 SEM images of nanoporous silver microstructures. A) The overall hexapod shape, B) nanopores.

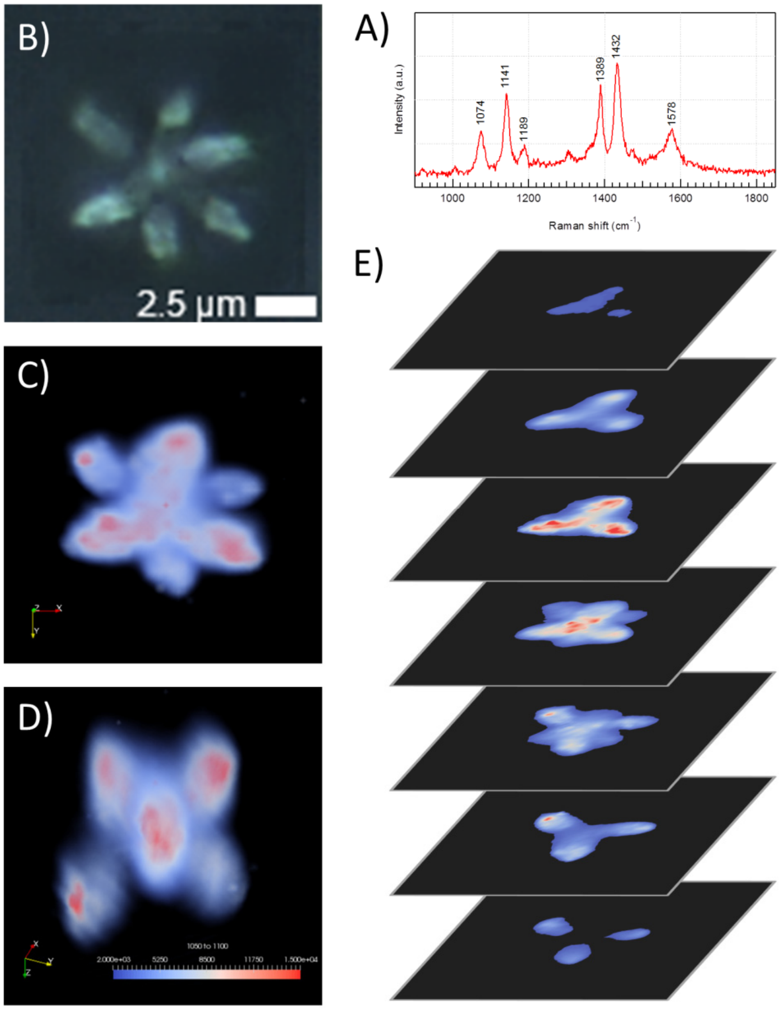

Figure 2 A) SERS spectra of PATP from the center of a hexapod silver microstructure. B) Optical microscope image of the particle. C),D) Top and diagonal views 3D SERS images constructed by PATP a1 mode at 1074 cm-1, using the same particle as B). E) 2D slices in the Z axis of B) with 1.5 µm separation per slice. Noted that C) and D) use the same color scale.

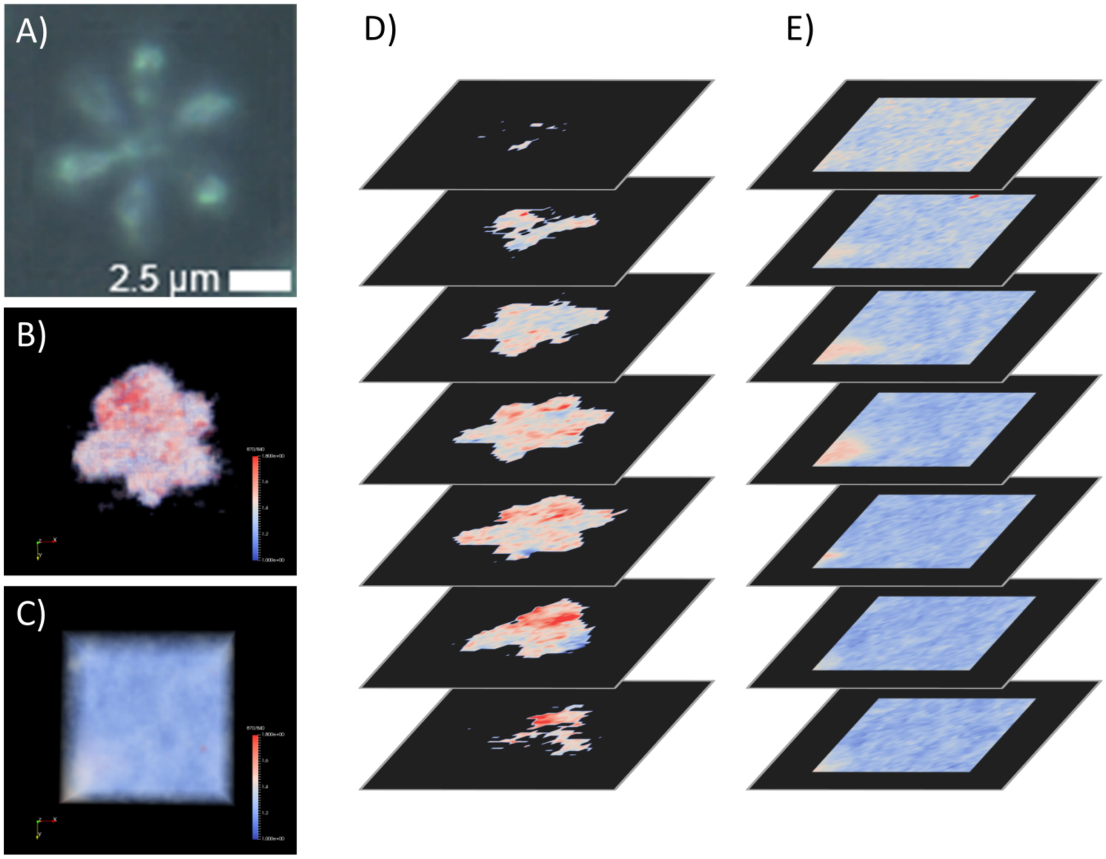

Figure 3 A silver microstructure in a PHB/PDLLA polymer blend. (A) The optical image. (B) 3D SERS imaging on the particle showing 870/840 cm-1 peak ratio. (C) 3D Raman imaging showing the same peak ratio but on the polymer outside the particle. (D), (E) 2D slices in Z axis with 1.0 µm separation per slice of (B) and (C), respectively.

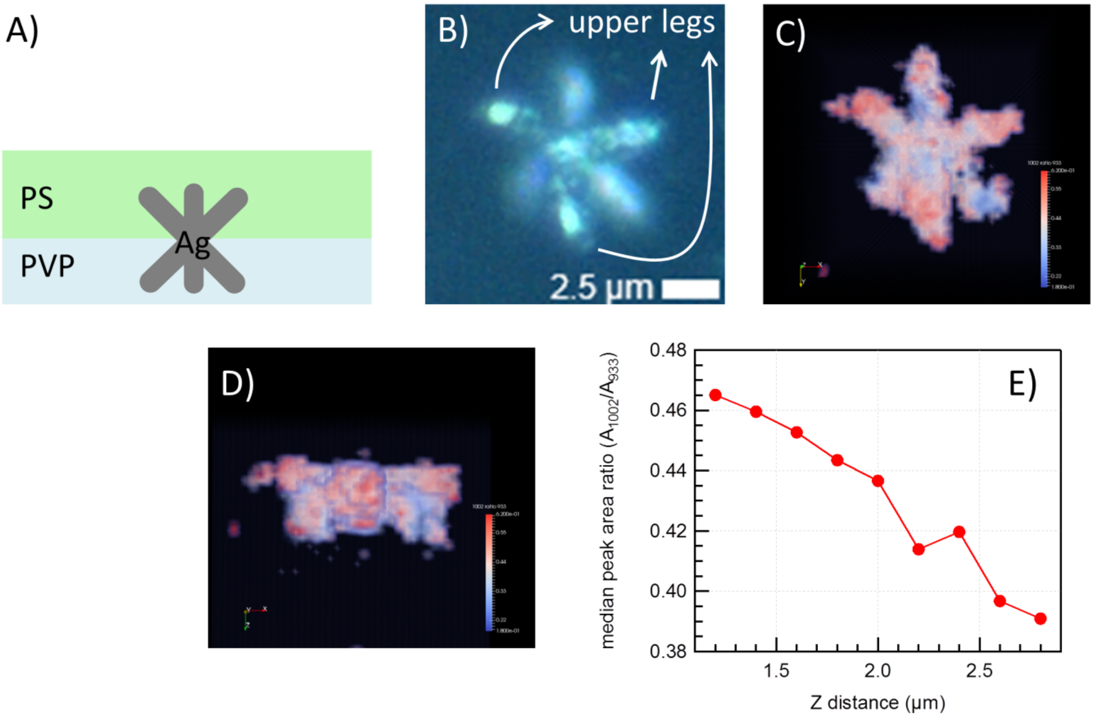

Figure 4 A) A Scheme represents a silver particle embedded in two-layer polymer system. B) Optical image of the silver particle in polymers. C),D) Top- and side-view 3D SERS images constructed by ratio between the peak area in the range of 990-1010 cm-1 and 910-955 cm-1 (representing the peak at 1002 cm-1 and 933 cm-1, respectively.). E) Median peak area ratio at each specific height, using the spectra from the particle only.

Acknowledgements

I would like to wholeheartedly express my gratitude to my advisor, Prof. Yukihiro Ozaki for deep academic advice, sincere suggestions, and fatherly care for the past three years. It was his effort, which made me grown up from a science student into a scientist.

Together with my advisor, Prof. Tadaaki Kaneko is undoubtedly the most important person for this research. Not only for the extremely high quality graphene samples from his laboratory, but also for teaching me about the perspective and attitude which a scientist should have. I also thank for Yasunori Kutsuma and Daichi Doujima for synthesizing the graphene samples and provide me great insights from the viewpoint of material science.

I would like to thank my mentors, Toshiaki Suzuki and Yasutaka Kitahama for teaching me about this research from the time when I still did not know anything about it. Both of them are truly kind bosses, smart scientists, nice co-authors, and great teachers. Thank you for Ryohei Hinaga for learning the TERS instrument together with me. I would like to thank Shohei Uemura with my sincere feeling for producing some crucial data for my publication. This work would not be completed without him. I also give my thanks to all Ozaki Lab members.

The thankfulness is undoubtedly extended to other co-authors of my publications: Tamitake Itoh, Shohei Uemura, Wang Mengfan, Harnchana Gatemala, Kanet Wongravee, and my master degree advisor, Prof. Sanong Ekgasit, for very insightful discussions. I learn so many things from them.

Thank you for my Japanese language teacher, Hisano Kirino, and also my close friends, Phiranuphon Meksiarun, Rapid Dong Chen, Paralee Puangchit, and Dian Marlina for kind supports and cheerful encouragements. They are certainly important persons who contribute in my happy life in Japan.

I would like to give my gratitude to Yoshida Scholarship Foundation, for providing a full PhD scholarship and The Office of International Affairs of Chulalongkorn Univeristy for inviting me to this scholarship. Because of this, I can solely focus on research and do not have to worry about my living cost. For research support, I would like to thank Kwansei Gakuin University for providing enough support system for my study and experiments.

Above all, I give the credit of everything I have done to my parents and my Lord Jesus Christ, who give me true love that nothing can replace.

List of publications

(1) Vantasin, S.; Tanabe, I.; Tanaka, Y.; Itoh, T.; Suzuki, T.; Kutsuma, Y.; Ashida, K.; Kaneko, T.; Ozaki, Y. Tip-Enhanced Raman Scattering of the Local Nanostructure of Epitaxial Graphene Grown on 4H-SiC $(000\bar{1})$. *J. Phys. Chem. C* **2014**, *118* (44), 25809–25815.

(2) Vantasin, S.; Tanaka, Y.; Uemura, S.; Suzuki, T.; Kutsuma, Y.; Doujima, D.; Kaneko, T.; Ozaki, Y. Characterization of SiC-Grown Epitaxial Graphene Microislands Using Tip-Enhanced Raman Spectroscopy. *Phys Chem Chem Phys* **2015**, *17* (43), 28993–28999.

(3) Vantasin, S.; Ji, W.; Tanaka, Y.; Kitahama, Y.; Wang, M.; Wongravee, K.; Gatemala, H.; Ekgaist, S.; Ozaki, Y. 3D SERS imaging using chemically-synthesized highly-symmetric nanoporous silver microstructure. *submitted to Angewandte Chemie*

List of related publications

(4) Vantasin, S.; Yan, X.; Suzuki, T.; Ozaki, Y. Tip-Enhanced Raman Scattering of Nanomaterials. *E-J. Surf. Sci. Nanotechnol.* **2015**, *13*, 329–338.

(5) Suzuki, T.; Itoh, T.; Vantasin, S.; Minami, S.; Kutsuma, Y.; Ashida, K.; Kaneko, T.; Morisawa, Y.; Miura, T.; Ozaki, Y. Tip-Enhanced Raman Spectroscopic Measurement of Stress Change in the Local Domain of Epitaxial Graphene on the Carbon Face of 4H-SiC(0001¯). *Phys. Chem. Chem. Phys.* **2014**, *16* (37), 20236–20240.

(6) Son, J.; Choi, M.; Choi, H.; Kim, S. J.; Kim, S.; Lee, K.-R.; Vantasin, S.; Tanabe, I.; Cha, J.; Ozaki, Y.; et al. Structural Evolution of Graphene in Air at the Electrical Breakdown Limit. *Carbon* **2016**, *99*, 466–471.

(7) Wongravee, K.; Gatemala, H.; Thammacharoen, C.; Ekgasit, S.; Vantasin, S.; Tanabe, I.; Ozaki, Y. Nanoporous Silver Microstructure for Single Particle Surface-Enhanced Raman Scattering Spectroscopy. *RSC Adv* **2015**, *5* (2), 1391–1397.